BRNO UNIVERSITY OF TECHNOLOGY

Faculty of Electrical Engineering
and Communication

MASTER'S THESIS

Brno, 2018 Bc. Eva Valterová

BRNO UNIVERSITY OF TECHNOLOGY
VYSOKÉ UČENÍ TECHNICKÉ V BRNĚ

FACULTY OF ELECTRICAL ENGINEERING AND COMMUNICATION
FAKULTA ELEKTROTECHNIKY
A KOMUNIKAČNÍCH TECHNOLOGIÍ

DEPARTMENT OF BIOMEDICAL ENGINEERING
ÚSTAV BIOMEDICÍNSKÉHO INŽENÝRSTVÍ

BLIND IMAGE DECONVOLUTION IN STEM MODE OF ELECTRON MICROSCOPE
SLEPÁ DEKONVOLUCE OBRAZU VE STEM MÓDU ELEKTRONOVÉHO MIKROSKOPU

MASTER'S THESIS
DIPLOMOVÁ PRÁCE

AUTHOR — **Bc. Eva Valterová**
AUTOR PRÁCE

SUPERVISOR — **Ing. Tomáš Potočňák**
VEDOUCÍ PRÁCE

BRNO 2018

BRNO UNIVERSITY OF TECHNOLOGY
FACULTY OF ELECTRICAL ENGINEERING AND COMMUNICATION

Master's Thesis

Master's study field **Biomedical and Ecological Engineering**
Department of Biomedical Engineering

Student: Bc. Eva Valterová ***ID:*** 167657

Year of study: 2 ***Academic year:*** 2017/18

TITLE OF THESIS:

Blind Image Deconvolution in STEM mode of Electron Microscope

INSTRUCTION:

1) Elaborate a literary research for blind image deconvolution. Study the definition of distortion parameters in scan mode of transversal electron microscop and its posible correction. 2) Design the procedure for optimal blind image deconvolution. 3) Design an evaluation procedure of the results and their dependence on acquisition parameters of the electron microscope. 4) Take pictures in collaboration with FEI Czech Republic. 5) Test the suggested methods on model and real images and compare them with the method available in Matlab - Image processing toolbox. 6) Discuss the results obtained and evaluate the effectiveness and usability of the methods. The diploma thesis is created in cooperation with FEI Czech Republic (part of Thermo Fisher Scientific).

RECOMMENDED LITERATURE:

[1] KARLIK M., Úvod do transmisní elektronové mirkoskopie. Praha ČVUT, 2011. ISBN 978-80-01-04729-3.

[2] CAMPISI, P., Egiazarian, K., Blind Image Deconvolution“ Theory and Applications. CRC Press: Boca Raton: 2007, 114 s. ISBN 978-1-4200-0729-9.

Date of project specification: 5.2.2018 ***Deadline for submission:*** 18.5.2018

Leader: Ing. Tomáš Potočňák
Consultant: Ing. Miloš Malínský, Ph.D.

prof. Ing. Ivo Provazník, Ph.D.
Subject Council chairman

Abstract

Blind image deconvolution is method, which restore the true image and point spread function simultaneously. The goal of this paper is to introduce several methods of blind deconvolution and find the optimal method for reconstruction of the true image and point spread function of images from scanning transmission electron microscope. The alternating minimization algorithm is assumed as the most convenient for blind deconvolution problem. Then it is modified and tested. The proposed algorithm properties are tested on artificially degraded data and the real data from scanning transmission electron microscope. The algorithm efficiency is evaluated by several evaluating criteria. The algorithm limitations are determined and its area of use is specified.

Keywords

Blind deconvolution, scanning transmission electron microscopy, blur, image restoration, point spread function, alternating minimization algorithm, total variation.

Abstrakt

Slepá dekonvoluce je metoda, při které je rozptylová funkce a skutečný obraz rekonstruován zároveň. Cílem této práce je představit různé metody slepé dekonvoluce a najít optimální metodu rekonstrukce původního obrazu a rozptylové funkce. Jako nejvhodnější metoda slepé dekonvoluce byl zvolen algoritmus střídavé minimalizace, který byl upraven a testován. Vlastnosti navrženého algoritmu byly testovány na uměle degradovaných datech a na reálných datech pořízených skenovacím transmisním elektronovým mikroskopem. Účinnost algoritmu byla hodnocena hned několika hodnotícími kritérii. Byla zjištěna omezení algoritmu a tím specifikováno jeho využití.

Klíčová slova

Slepá dekonvoluce, skenovací transmisní elektronová mikroskopie, zkreslení, restaurace obrazu, rozptylová funkce, střídavý minimalizační algoritmus, totální variace.

Declaration

I declare that I have written my master's thesis titled "Blind Image Deconvolution in STEM mode of Electron Microscope" independently, under the guidance of the supervisor and using technical literature and other sources of information which are all quoted in the thesis and detailed in the bibliography at the end of the thesis.

As the author, I furthermore declare that, with respect to the creation of this thesis, I have not infringed any copyright or violated anyone's personal and/or ownership rights. In this context, I am fully aware of the consequences in the case of breaking Regulation §11 and the following Copyright Act No. 121/2000 Coll., and of the rights related to intellectual property right and changes in some Acts (Intellectual Property Act) and formulated in later regulations, inclusive of the possible consequences resulting from the provisions of Criminal Act No. 40/2009 Coll., Section 2, Head VI, Part 4.

Brno …… ……..
Eva Valterová

VALTEROVÁ, E. *Slepá Dekonvoluce Obrazu ve STEM Módu Elektronového Mikroskopu* Brno: Vysoké učení technické v Brně, Fakulta elektrotechniky a komunikačních technologií, 2018. 60s. Vedoucí diplomové práce Ing. Tomáš Potočňák.

Acknowledgement

I would like to thank my supervisor Ing. Tomáš Potočňák and my consultant Ing. Miloš Malínský, Ph.D., for kind and valuable help and the professional advice. I would also thank the FEI Czech Republic, s. r. o. company for the opportunity of collaboration and for providing the data. My special thanks belong to my family, friends for advice and support during all my university studies.

Brno …… ……..
Eva Valterová

Contents

List of figures

Introduction

The transmission electron microscope (TEM) was invented in 1932 by Knoll and Ruska. This invention has proven to be very useful and beneficial for very high resolution observation of samples. Several years later Manfred von Ardenne (1938) noticed the great potential of scanning sample by focused probe within the rectangular frame. This idea was successfully realized many years later (1966), with the development of the scanning transmission microscope (STEM). Since then STEM has gone through many improvements [1].

Nowadays, STEM can be regarded as a powerful operation mode, but images of sample from the STEM are still burdened by degradation. The degradation originate because of imperfections of microscope construction. The first one has a random nature and appears in images as noise and the second one is deterministic and results in blurring. The blurring of the image is modelled by convolution of true image and point spread function (PSF).

This paper introduces an inverse problem - blind image deconvolution, where outputs are given (observed image) and inputs (true image and PSF) are sought. Some commonly used method for solving the blind deconvolution problem are introduced. The method of fast alternating minimization is chosen as the most optimal method for the STEM images. For image regularization is used total variation regularization. The algorithm is evaluated on both test data and real data. Furthermore, it is compared with the built-in Matlab function *'deconvblind'*. The algorithm results on the test data are evaluated using the root mean square error value and structural similarity index measure. The algorithm efficiency on the real data is measured by sharpness and contrast measurement.

This paper is organized as follows. Section 1 refers about TEM construction. STEM mode of TEM is described in section 2. Section 3 describes image degradation parameters. Section 4 introduces several blind deconvolution methods and in Section 5 is the proposed methodology. Results and conclusion of this paper are in Section 6 and Section 7, respectively.

1 Transmission electron microscope (TEM)

Light microscopy uses visible light as a source of illumination and optical glass lenses to magnify specimens in an approximate range between 10 to 1,000 times their original size. The resolution of light microscopes is limited by the diffraction limit, which is equal to half of the wavelength of the used light. In contrast to light microscopy, electron microscopy uses a beam of electrons to form an image of a specimen and electromagnetic lenses to magnify specimen. Electrons could be accelerated and thus reach shorter wavelength than visible light. Electron microscopes, therefore, have a better resolving power. The two basic types of electron microscopes are the scanning electron microscope (SEM) and the transmission electron microscope (TEM) [2].

1.1 Construction

A transmission electron microscope consists of an electron source and a lensing system which focuses the beam on the specimen and projects it onto the viewing screen. A part of the electron microscope is also a vacuum system, which provides various levels of vacuum in the microscope tube. Vacuum is necessary to provide free electron path, to isolate electron filament and to avoid contamination of the sample by molecules of air [2].

1.1.1 Electron gun

The illumination electrons are produced by an electron gun, which consists of three parts – the filament (cathode), the shield, and the anode. The requirements of the electron gun are a low span of emission electrons energy, high intensity of electron beam in a small space angle, low noise, enduring stability, and a small size of the gun. There are two major types of the electron guns which differ in the emission mechanism and properties as brightness, spot size, electron energy dispersion or required vacuum level, and others [2].

The first is thermionic electron gun (see Figure 1 – left), which uses the principle that as certain materials are heated, the electrons in the outer orbitals become unstable and start to leave the surface of the filament. The filament is most commonly made of tungsten (eventually of LaB_6 – lanthanum hexaboride) and bent into a tip. Because of the bending in a single plane the region of emission is not perfectly circular. This problem can be reduced by attaching a finely pointed crystal to a tip of the filament. The electron beam is further pre-focused by a shield (Wehnelt cylinder). Then the electrons emitted from the

filament are drawn away by the anode plate which is a large circular plate with a central opening or aperture [3].

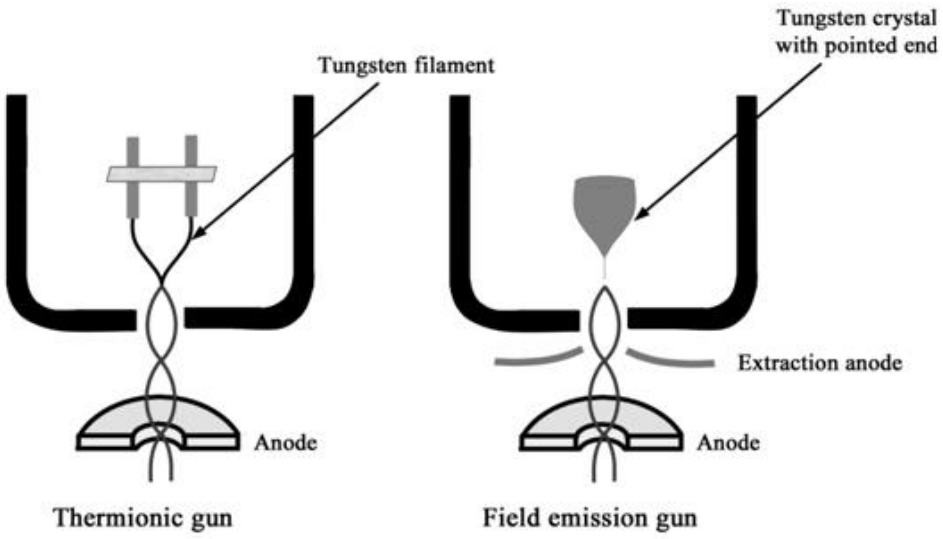

Figure 1: The systhematic schema of gun [4]

The second type of electron gun is the autoemission gun which operates on the principle of quantum tunnelling. Emitters are either of cold cathode type (field emission) or of the Schottky type. The Schottky emitter type uses an increased temperature, in the presence of a high electric field, to lower barrier to electron emission. A field emission gun (Figure 1 - right) filament is not heated to extract electrons, instead the electrons are drawn away by an intense potential field created by an extraction anode. In this case, the region of emission is very small and is often aided and accelerated by a second anode. The field emission gun achieves a smaller electron beam diameter, which is more coherent and with up to three orders of magnitude greater current density or brightness than can be achieved with conventional thermionic emitters (Table 1: Gun comparison Table 1). These advantages make the field emission gun appropriate for microanalytical applications in a scanning transmission electron microscopy [5].

Table 1: Gun comparison [5]

Cathode	Thermionic		Autoemission	
	Tungsten filament	LaB_6	Schottky	Field emission
Brightness [$A \cdot m^{-2} \cdot sr^{-1}$]	10^9	10^{10}	$5 \cdot 10^{12}$	10^{11} - 10^{13}
Apparent source size [µm]	50	10	0,03	0,005
Electron energy dispersion [eV]	3	1,5	0,3 - 1	0,3
Working temperature [K]	2700	1900	1800	300
Vacuum [Pa]	10^{-3}	10^{-5}	10^{-6} – 10^{-7}	10^{-8}

1.1.2 Magnetic lenses

Transmission electron microscopes generally use three stages of lensing. The electrons from the filament first go through the condenser lenses, which form the primary beam and focus it onto the sample to give uniform illumination. The objective lens is the second stage of the lensing system. These form the initial enlarged image of the illuminated portion of the specimen in a plane that is suitable for further enlargement by projector lens. The last stage of the lensing system consists of projector lenses, which finally project the image onto the detector. It is difficult to achieve a perfect image because the lenses are not perfect which causes defocusing of the probe. These effects are called aberrations and will be discussed later [5].

1.1.3 The specimen stage

A specimen stage is placed inside the objective lens. A stage is required in order to have the ability to hold a very small specimen in precisely the correct position and also be capable of moving several millimeters and tilting by a large angle (up to ± 70°). The specimen stage is realized as a specimen rod with an interchangeable standardized grid upon which a sample is placed [5].

1.1.4 Imaging system

Electrons transmitted through the sample and focused by the objective and projective lenses are captured by the detector.

In bright field and annular dark field modes (explained later in chapter 2) the detector utilize a silicon substrate with an epitaxy layer on the top. This detector operates on the p-n junction principle of both materials. Increasing the electron intensity signal increases the detected current [6].

High-angle annular dark-field mode uses an inorganic scintillator made of YAP – Yttrium aluminum Perovskite activated by Ce^{3+}. Its advantage is a very fast response time compared to a zinc sulfide phosphor screen. YAP single crystals convert electrons to photons, which are transported to a photomultiplier tube and later amplified and digitalized [7].

2 Scanning transmission electron microscopy (STEM)

A scanning transmission electron microscope is a type of transmission electron microscope. The main difference is in sample scanning. The electron beam is focused to a spot as small as possible and scans the sample within a rectangular frame. The focal point of the objective lens defines the STEM probe. If the focal point of the lens is blurred due to some aberrations, the STEM probe becomes larger [1].

The transmitted electrons provide the image of the sample and an additional signal could be also collected from secondary electrons, backscattered electrons or X-rays.

There are three modes of electron detecting, which differ in the location of where the signal from electrons is collected (Figure 2). It is bright-field (BF), annular dark-field (ADF) and high- angle annular dark-field (HAADF). The bright-field detector collects transmitted electrons that travel in a straight path. For the case where there is no scatterer in the path of the beam, the BF signal is approximately equal to the total beam current [1]. The annular dark-field signal displays the scattering power of the object that is in the path of the beam for the selected angular range. The scattering power increases with the thickness of the specimen. The HAADF is often used in cases, where the collected electrons are scattered to high angles.

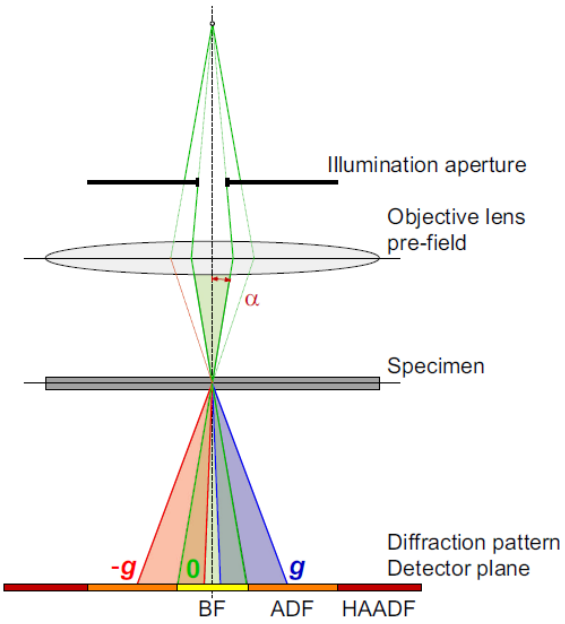

Figure 2: A schematic diagram of a STEM [1].

It is possible to form atomic resolution images, where the contrast is directly related to the atomic number by using STEM and a high-angle detector [8].

3 Aberrations of optical imaging systems

The observed image could differ from the true image. Distortions are influenced by the parameters of the system, such as electron lens aberrations, the coherency of the electron beam, noise and stability of the electromagnetic lens fields, diffraction and others. The following chapters explain in more detail the mentioned artefacts.

3.1 Electron lens aberrations

Electron lens imaging is most influenced by the following optical aberrations – the spherical aberration, chromatic aberration, astigmatism and coma.

3.1.1 Spherical aberration

Spherical aberration causes the focal point of rays coming from a point source on an optical axis and passing the lens farther from the source axis to be displayed nearer the lens than rays passing the center. The probe size is limited by spherical aberration and the smallest achievable probe is called the disk of least confusion δ_S (Figure 3).

The best way to reduce the effects of this aberration is to cut off the most outlying part of the lens by reducing aperture. In STEM the corrector of spherical aberration is placed ahead of the objective rather, then behind it like in TEM [1] [9].

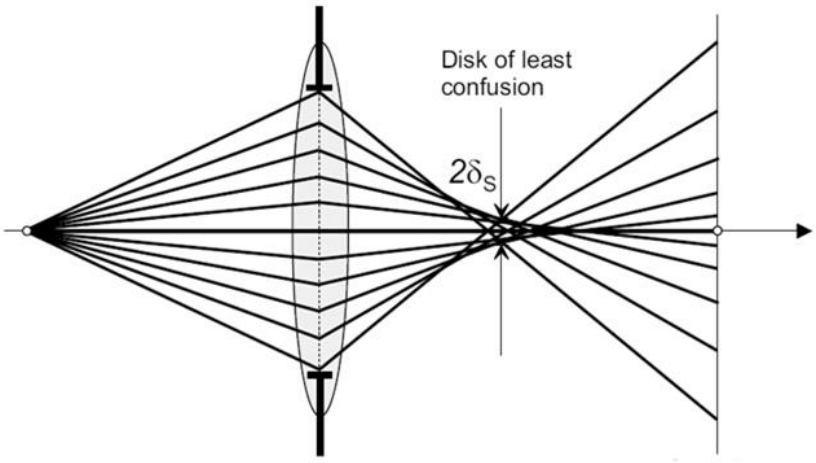

Figure 3: Spherical aberration - δ_S – the disk of least confusion [1]

3.1.2 Chromatic aberration

A consequence of the real source instability, electron source emits electrons of varying energy. Further, some electrons lose part of their energy in interaction with the specimen. The lower/higher energy electrons passing through the electromagnetic lens have a focal point either closer/farther from the lens than the focal point of the nominal source energy

electrons. The smallest achievable probe size, limited by chromatic aberration, is expressed by the disk of least confusion δ_C (Figure 4). The diameter of chromatic aberration increases with the opening of the aperture. To fix the defect it is recommended to use a monochromator, make the sample as thin as possible, and eventually add a filter to remove the inelastically collided electrons [1] [9].

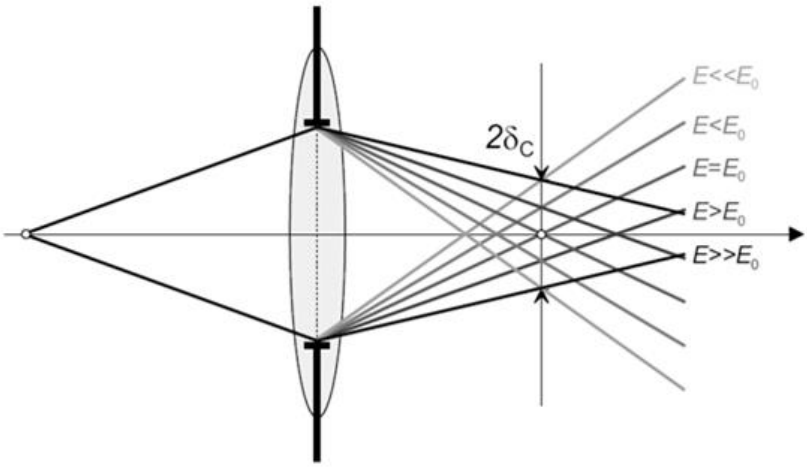

Figure 4: Chromatic aberration - δ_C – the disk of least confusion [1]

3.1.3 Astigmatism

Astigmatism results in different focal points for rays travelling in the horizontal plane and for rays travelling in the vertical plane (Figure 5). Astigmatism is corrected by adding an extra magnetic field of a stigmator that compensates for the heterogeneities [1] [3].

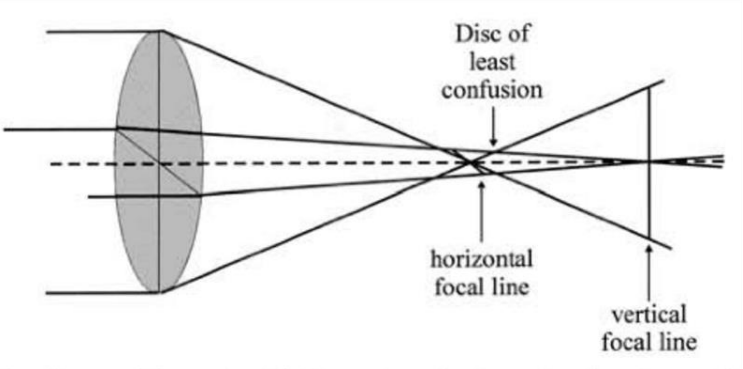

Figure 5: Astigmatism [3]

3.1.4 Coma

Coma is the optical deformation of an image point located in the subject plane out of the optical axis and illuminated at an angle, resulting in a distortion shape similar to a comet (Figure 6). The aberration increases with the angle under which the object point rays pass the aperture, terminating in a circle visible in the image plane with a radius proportional to a third-order coma coefficient and the lateral magnification [1].

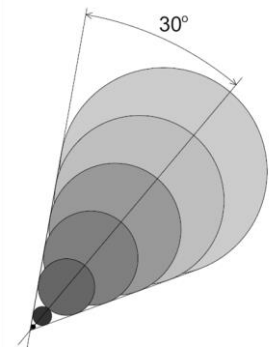

Figure 6: Specific coma figure [1]

3.2 Diffraction

The electron probe gives an imperfect representation of the electron source image. One of the factors causing this distortion is the presence of an aperture, limiting the angular range of the illuminating electrons. Nevertheless, an aperture of finite size is needed to optimize the size of the electron probe in order to decrease the influence of lens aberrations. If the aperture is illuminated by a parallel beam, diffraction occurs and the electron probe at the object plane appears as an Airy pattern. An Airy pattern can be identified as a central bright region with a series of concentric rings of decreasing intensity. The electron probe radius size δ_D is dependent on the size of the aperture and is expressed by

$$\delta_D = 0{,}61\frac{\lambda}{\alpha}, \tag{1}$$

where α is a semi-angle defined by the aperture opening (shown in Figure 2) and λ is the electron wavelength. From this equation, it follows that the aperture opening diameter is inversely proportional to the electron probe diameter [1].

3.3 Electron probes

The electron probe size determines the resolution of the STEM. That means that two objects closer than the size of the probe cannot be recognized as distinct. Thus the goal is to have as small a probe as possible. Also, since the size of the electron probe is directly correlated with aperture, the geometrical aberrations are reduced with decreasing size. Unfortunately, diffraction effects increase with decreasing aperture, thus it becomes necessary to optimize the size of the probe according to the amount of aberrations and degree of diffraction (Figure 7) [10].

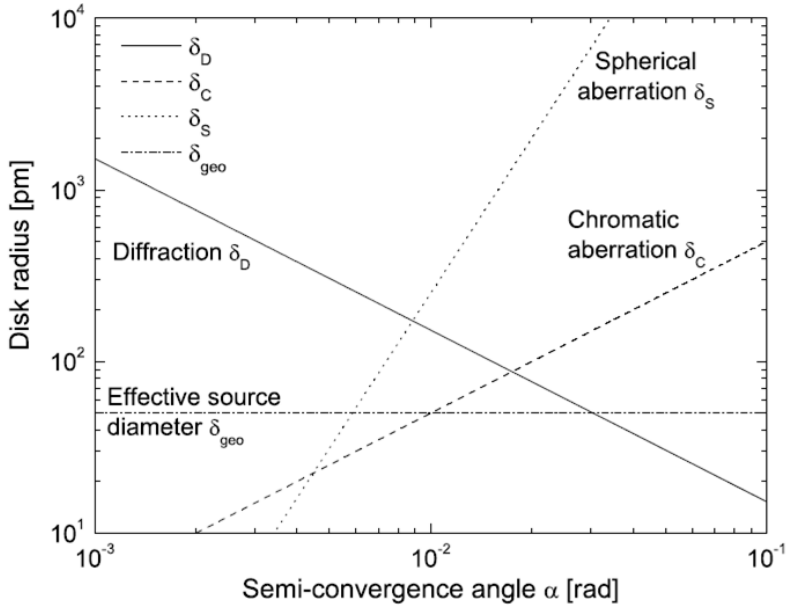

Figure 7: Dependency of the effective source diameter, the chromatic aberration, the spherical aberration and the diffraction limit on the illumination semi-angle [1]

Furthermore, the probe, influenced by diffraction, the spherical and chromatic aberrations, is not solely considered as a two-dimensional spot, but as a three-dimensional intensity distribution.

4 Blind deconvolution

As a consequence of many different effects and distortions (e. g. optical aberrations, additive noise, …), the observed image differs from the true image. Degradations can be modelled as the true image $f(x)$, convoluted with an unknown point spread function (PSF) and contaminated by additive noise $n(x)$ (Figure 8). This model is referred to as a linear degradation system (LDS) and is linear and space invariant [11].

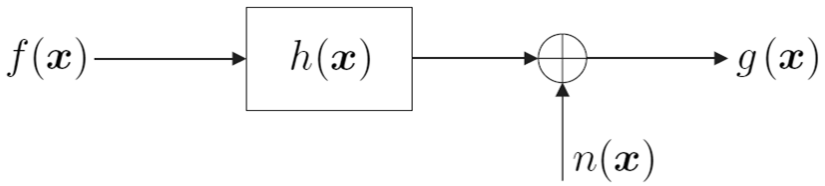

Figure 8: LDS - $h(x)$ – convolution of $f(x)$ and PSF, $g(x)$ – observed image

The equation form of this model is expressed by

$$f * h + n = g \,. \tag{2}$$

However, reconstruction of the true image is an inverse problem. The goal of deconvolution is to split the true image from the PSF. Unfortunately, sometimes the PSF is unknown or only partially known and needs to be estimated. Through blind deconvolution (BD) the goal can be achieved.

4.1 Blind deconvolution methods

The blind deconvolution is widely used across many different technical areas, including medical imaging, optics, remote sensing, astronomical imaging and microscopy among others. Thus many methods have been proposed for solving the problem of an unknown PSF. These methods can be subdivided according to the phase at which the blur is identified [11].

4.1.1 Prior PSF identification methods

The PSF is identified independently on the true image and is then applied to other images for deconvolution using one of the classical image restoration methods.

The PSF from the true image could be found in two ways. The first option is to determine it from the real underlying image that is known. For example, such could be an image of stars in astronomy, which are supposed to be point sources, edge detection in x-ray imaging or prediction of sharp edges [12]. This method neglects the additive noise [11].

The second way is to make a prediction of the blur based on known parameters of the imaging system and its aberrations. This approach is limited by the presence of noise.

In many applications, it is difficult to characterize the PSF, because of the time dependency of the function. It is often impossible to get a known image or estimate all the relevant parameters of the imaging system precisely. Due to this, most of the blind deconvolution methods belong to the next group.

4.1.2 Joint PSF identification methods

In these methods, the PSF and the true image are identified simultaneously. These methods solve the problem of unknown degradation and noise which influence the resulting blur. The following chapters will introduce and elaborate on some of the most commonly used methods [11].

4.2 Zero sheet separation

Zero sheet separation is built off a Z- transform and the assumption is that there is no additive noise in the imaging system [13]. This method provides valuable insight into the BD problem in multiple dimensions, but it also has many disadvantages such as high sensitivity to noise, computational complexity, and numerical inaccuracy for large data sizes [14].

The method is defined as

$$G(z_1, z_2) = F(z_1, z_2)H(z_1, z_2)\,, \tag{3}$$

where capital letters label Z-transform of the true picture f, the blur h and the observed image g [15]. The solution of this equalization rests on the proven premise that any signal formed by multiple convolutions is automatically deconvolutable provided it has a dimension greater than one.

4.3 ARMA parameter estimation method

The ARMA parameter estimation method identifies the PSF and the true image using an autoregressive moving average (ARMA) process [11]. The true image $f(x, y)$ is modelled by a two-dimensional autoregressive (AR) process expressed by

$$f(x, y) = \sum_{\substack{(l,m)\in R_a \\ (l,m)\neq(0,0)}} a(l, m)f(x - l, y - m) + v(x, y)\,, \tag{4}$$

where $a(l, m)$ are model coefficients equal to 1 in $a(0,0)$, and $v(x, y)$ is the modelling error represented by zero-mean homogeneous noise.

The PSF $h(x,y)$ is modelled by a two-dimensional moving average (MA) process represented by:

$$g(x,y) = \sum_{(l,m)\in R_h} h(l,m) f(x-l, y-m) + n(x,y)\ , \tag{5}$$

where $n(x,y)$ is the additive noise of the imaging system. The model of the ARMA method is given in the following schema (see Figure 9), where capital letters label Z-transforms of their lowercase counterparts. The goal of this method is to estimate model coefficients $a(l,m)$ and PSF $h(x,y)$. For estimating the ARMA parameters it is possible to use the maximum-likelihood (ML) estimation [16], generalized cross-validation, or neural networks [17].

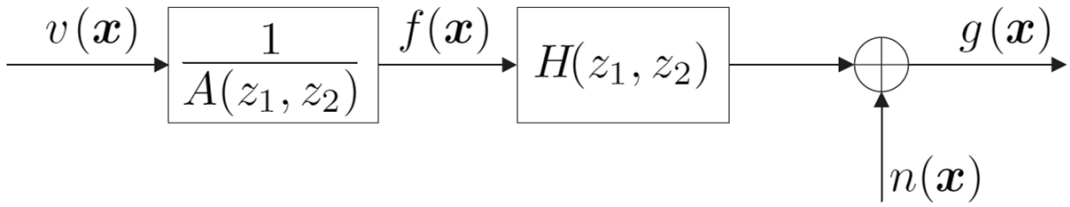

Figure 9: ARMA degradation model

4.3.1 Maximum likelihood estimation

Maximum likelihood estimation provides an estimate of the parameter values which maximize the likelihood of making the observed image g given the parameter set (f,h).

$$f = \arg\left\{\max\ p(g|f,h)\right\}, \tag{6}$$

The ML is used for estimation ARMA model. This estimation is sensitive to noise, but insensitive to changes in the individual parameters when the total number of parameters is large.

4.4 Regularization

Image deconvolution is an inverse problem where the outputs are given and the inputs are sought. In addition, the problem is ill-posed if one of the following is true:

1. a solution does not exist
2. a solution is not unique
3. the solution's behaviour does not change continuously with the inputs

To stabilize the problem constraints (regularizations) are introduced and a cost function is incorporated. The goal of introducing these is to minimize the cost energy function, which is designed to accommodate assumptions about the true image as well as the degradation model [18]. There are many forms of constraints described in individual

methods such as the Tikhonov regularization method, total variation method, dynamical system methods or Gauss-Newton iteration, just to name few.

4.4.1 Least squares method

This regularization method is built on the least squares method. The resultant image is determined by the global minimum of the cost function(E). This could be expressed by

$$E(u) = \|Hu - g\|_2^2 \,, \tag{7}$$

where H is a degradation operator, u is the true image and g is the observed image [19].

4.4.2 Tikhonov regularization

Using the least squares method with an ill-posed inverse problem causes an issue which could be solved by the Tikhonov regularization

$$E(u) = \|Hu - g\|_2^2 + \lambda^2 \|Lu\|_2^2 \,, \tag{8}$$

where L is an approximation of the derivative and parameter λ is a non-negative weighting factor to control the strength of the regulation constraint [19]. The resultant image is again attained by the global minimum of the cost function. In spite of computational advantages, this method generally results in over-smoothing which limits its application.

4.4.3 Total variation regularization

Total variation regularization (TV) preserves sharp discontinuities but loses the fine scale. This method helps to restrict the set of possible solutions to those having a sparse gradient [20]. TV is formulated by the expression

$$E(u) = \|Hu - g\|_2^2 + \lambda^2 \|Lu\|_2 \,, \tag{9}$$

where the variables have the same meaning as previously defined [21].

4.5 Iterative blind image deconvolution

Definition: "An iterative algorithm is one that takes an initial input, approximates the output, then takes this approximation as an input and repeats to create a sequence of approximations that converge toward the true solution." [22]

In the application of the Tikhonov regularization and the TV method it is assumed that the PSF is known, but generally, it is unknown. To estimate both, the true image and the PSF, it is possible to use the iterative blind image deconvolution described in Figure 10. In the first iteration, it would be assumed that the observed and true images are equal and PSF is a Dirac unit impulse (step 1.). In the next step, the PSF is updated using Fourier

domain and some prior knowledge about the true image (steps 2-3). The new values are then applied to change the PSF and determine a new approximation of the true image (steps 5-7). Every new estimate of PSF and the true image are imposed by plane constraints (steps 4 and 8).

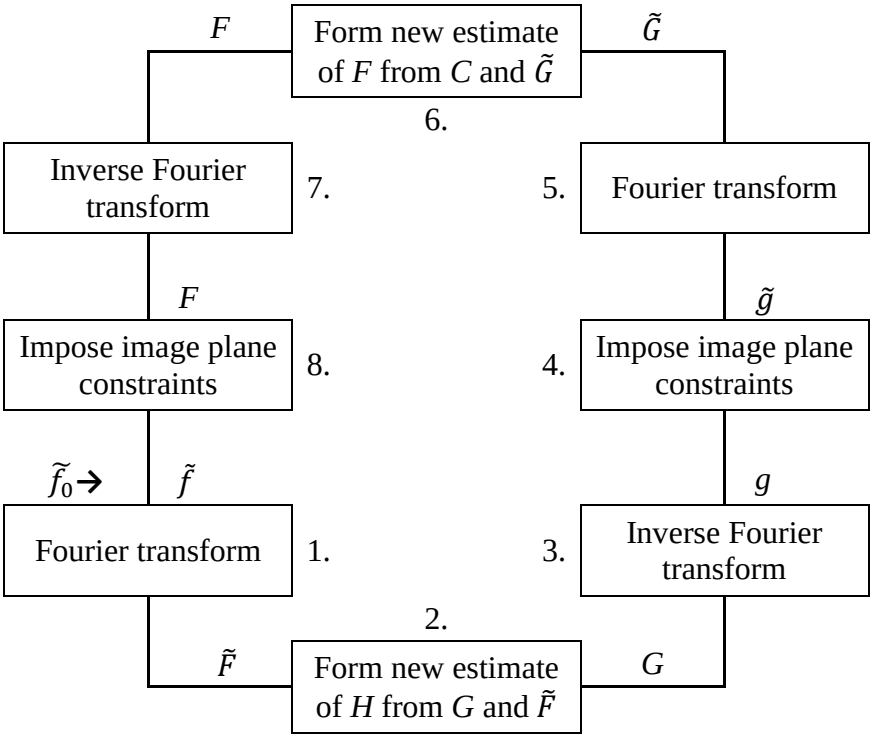

Figure 10: Schema of the deconvolution algorithm

The iterative method has low computational complexity and robustness to noise. Another advantage is the possibility of many different implementations, which could differ in their assumptions about PSF and the true image and how these assumptions are imposed on the image. One of the drawbacks is sensitivity to the initial image estimate and later possible instability [23].

4.6 Simulated annealing algorithm

This algorithm is the same as the one described in the iterative blind image deconvolution, with the difference that simulated annealing assumes a positive PSF with known finite support and attempts to minimize the cost function. If some iteration leads to a decrease in the cost function, the parameter estimates are accepted, however, if it leads to an increase, the parameters are replaced with the probability function

$$p = e^{\frac{-\Delta J}{T_k}}, \tag{10}$$

where ΔJ is the difference in the cost function and T_k is the temperature parameter [24]. The temperature decreases with increasing number of iterations.

5 Proposed method for STEM

Another method for solving blind deconvolution problem is robust blind deconvolution via alternating minimization (AM). The proposed method is based on the same idea as in [25], where multiple images are considered, but it is modified for single-channel case. This method assumes a space-invariant blur and can handle very large blurs and images in order of several megapixels.

Vector-matrix notation is used throughout the text. The PSF and the images are represented by small italic letters and their corresponding vectorial representations are denoted by small bold letters. Hence, the equation

$$g = u * h + n \,. \tag{11}$$

where g denotes input observed images, h an unknown blur, u an unknown true image and n is additive noise, could be expressed

$$\boldsymbol{g} = \boldsymbol{H}\boldsymbol{u} + \boldsymbol{n} = \boldsymbol{U}\boldsymbol{h} + \boldsymbol{n} \,.$$

Where $\boldsymbol{H}$ and $\boldsymbol{U}$ denote convolution with h and u respectively.

As has been said before to resolve the ill-posed problem it is necessary to introduce some sort of regularization. The total variation is used for image regularization (Q). This optimization problem is expressed by

$$\min_{u,\{h\}} F(u,\{h\}) + Q(u) \,, \tag{12}$$

where F is the data fidelity term, u denotes the true image and h the unknown blur (PSF). The solution would be sought by alternate optimizing and by splitting into two steps.

$$\text{“}u\text{- step”}: \quad \min_{u} F(u,\{h\}) + Q(u) \tag{13}$$

$$\text{“}h\text{- step”}: \quad \min_{h} F(u,\{h\}) \tag{14}$$

Image regularization Q is written as

$$Q(\boldsymbol{u}) = \phi\left(\boldsymbol{D}_x\boldsymbol{u}, \boldsymbol{D}_y\boldsymbol{u}\right) = \sum_i \sqrt{[\boldsymbol{D}_x\boldsymbol{u}]_i^2 + \left[\boldsymbol{D}_y\boldsymbol{u}\right]_i^2} \,, \tag{15}$$

where $\boldsymbol{D}_x$ and $\boldsymbol{D}_y$ are matrices representing derivatives with respect to x and y.

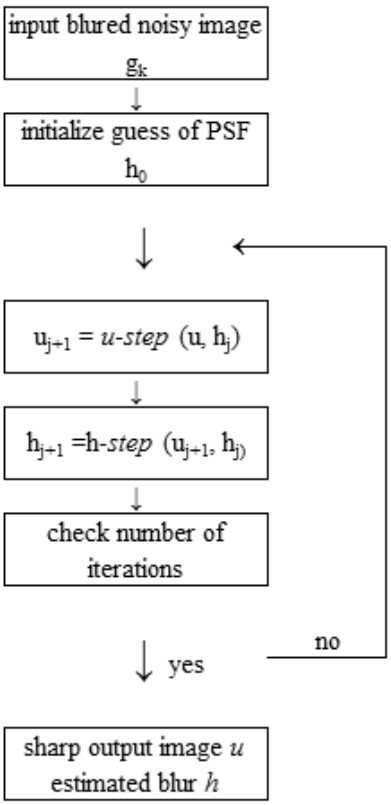

Figure 11: Flowchart of the alternating minimization algorithm

5.1 Optimization process

The main loop of the algorithm is described in Figure 11, where j denotes iteration number. The initial estimate of the PSF and definition of parameters α and γ is required before the main iteration loop. The iteration loop consists of two subproblems: minimization with respect to the image *u*-step and *h*-step.

5.1.1 *U*-step

U-step is realized by following equations

$$\boldsymbol{u}^{j+1} = \frac{\boldsymbol{H}^T\boldsymbol{g} + \left(\frac{\alpha}{\gamma}\right)\left[\boldsymbol{D}_x^T\left(v_x^j + a_x^j\right) + \boldsymbol{D}_y^T\left(v_y^j + a_y^j\right)\right]}{\boldsymbol{H}^T\boldsymbol{H} + \left(\frac{\alpha}{\gamma}\right)\boldsymbol{D}_x^T\boldsymbol{D}_x + \boldsymbol{D}_y^T\boldsymbol{D}_y}, \tag{16}$$

where

$$\left[v_x^{j+1}\right]_i = \left[\boldsymbol{D}_x\boldsymbol{u}^{j+1} - a_x^j\right]_i [s]_i^{-1} \max\left([s]_i - \frac{1}{\alpha}, 0\right), \tag{17}$$

$$\left[v_y^{j+1}\right]_i = \left[\boldsymbol{D}_y\boldsymbol{u}^{j+1} - a_y^j\right]_i [s]_i^{-1} \max\left([s]_i - \frac{1}{\alpha}, 0\right), \tag{18}$$

$$[s]_i = \sqrt{\left[\boldsymbol{D}_x \boldsymbol{u}^{j+1} - a_x^j\right]_i^2 + \left[\boldsymbol{D}_y \boldsymbol{u}^{j+1} - a_y^j\right]_i^2}, \tag{19}$$

$$a_x^{j+1} = a_x^j - \boldsymbol{D}_x \boldsymbol{u}^{j+1} + v_x^{j+1}. \tag{20}$$

$$a_y^{j+1} = a_y^j - \boldsymbol{D}_y \boldsymbol{u}^{j+1} + v_y^{j+1} \tag{21}$$

For first iteration is $v_x^0 = v_y^0 = a_x^0 = a_y^0 = 0$ and index i denotes individual pixels.

5.1.2 *H*-step

H-step consists of only one equation:

$$\boldsymbol{h}^{j+1} = \frac{\boldsymbol{U}^T \boldsymbol{g}}{\boldsymbol{U}^T \boldsymbol{U}}. \tag{22}$$

The stopping criterion suggested in [25] of the whole loop is defined as:

$$\left\|\boldsymbol{h}^j - \boldsymbol{h}^{j-1}\right\| / \left\|\boldsymbol{h}^j\right\| < tol. \tag{23}$$

Within every *u*-step and *h*-step are used constraints introduced by *Ayers and Dainty* [23]. These constraints are expressed by the following equations

$$\tilde{f}_i(x) = f_i(x) \qquad \text{for} \quad f_i(x) \geq 0 \tag{24}$$

$$\tilde{f}_i(x) = 0 \qquad \text{otherwise} \tag{25}$$

Where $f_i(x)$ denotes the primary image and $\tilde{f}_i(x)$ denotes its transformation. In our case this transformation is implemented on *u*-step and *h*-step, thus the variables are respectively replaced.

The correction of energy redistribution needs to be done after this transformation by

$$E = \int_{-\infty}^{+\infty} \left[f_i(x) - \tilde{f}_i(x)\right] \mathrm{dx} \tag{26}$$

$$\tilde{f}_i(x) = \tilde{f}_i(x) + \frac{E}{N} \tag{27}$$

where E is the sum of the function's negative values and N is the number of the image's pixels. Those constraints for *u*-step and *h*-step are implemented because non-negative values in the image and the PSF are required. The algorithm also achieves better results after constrains implementation. Furthermore, several repeating *u*-steps within one iteration of *h*-step are implemented for further improvement of the estimated image.

5.2 Solution structure

The proposed algorithm is compared with the built-in Matlab function. Both algorithms are tested on the test data and the real data from the STEM. First, the test data is blurred and the noise is added. Then the true image of the test data is estimated using blind

deconvolution algorithms and the results are evaluated. The next step is to apply both algorithms on real data and evaluate the results.

5.3 Test data blurring and noise adding

In general, the observed degradation is caused by two physical phenomena.

The first phenomenon is deterministic and results in blurring. This degradation of the image is modelled by convolution of test data and matrix of kernel size. The brightness of the blurring matrix is given by the Gauss distribution expressed by

$$g(x) = \frac{1}{\sigma\sqrt{2\pi}} e^{-\frac{1}{2}\left(\frac{x-\mu}{\sigma}\right)^2}, \tag{28}$$

where σ is the variance and μ is the expected value. Three different kernel matrix sizes (5x5, 9x9, and 13x13 pixels) with two various values of parameter σ are shown in Figure 12 and Figure 13. The original test image (true image) and Gauss matrix convolution cause image smoothing, which increases with parameter sigma. The examples of blurred test data are shown in Figure 14. Figure 15 and Figure 16 show the detail of one line of the blurred test data.

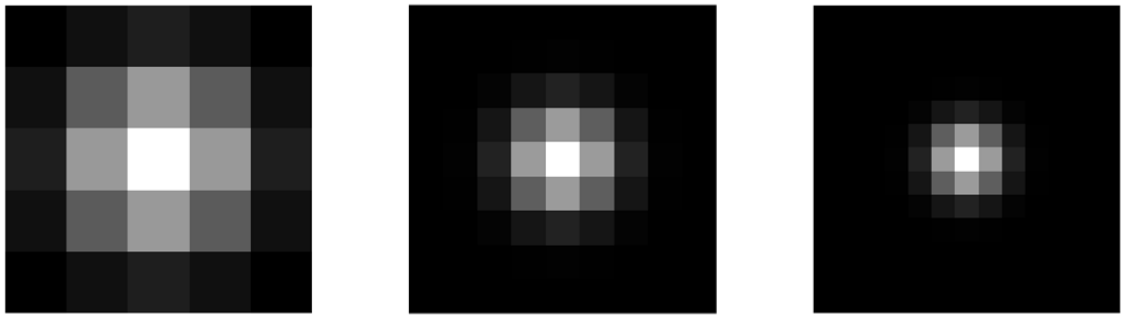

Figure 12: Matrix of kernel size 5x5, 9x9 and 13x13 with σ = 1

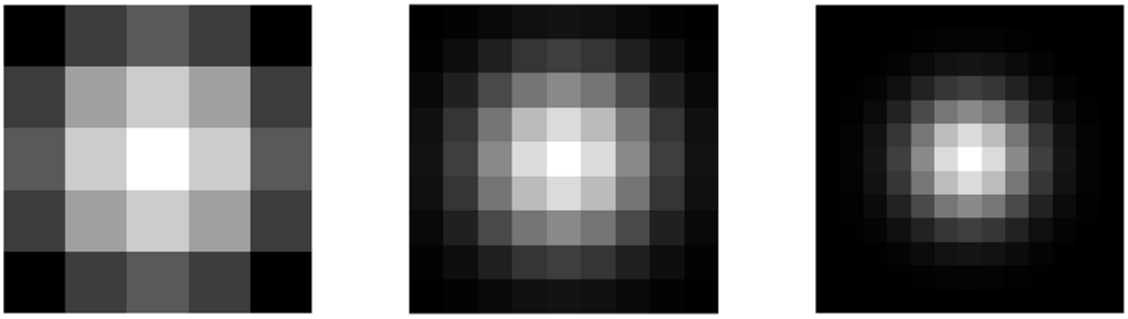

Figure 13: Matrix of kernel size 5x5 , 9x9 and 13x13 with σ = 1.8

The second one is of a random nature and appears in images as noise. Hence, Gaussian white noise is added to the test data. The noise mean value is set to zero and variance σ_n^2 is expressed from equation

$$SNR = 10\ \log_{10}\left(\frac{\sigma_s^2}{\sigma_n^2}\right), \tag{29}$$

where SNR label noise level in decibels and σ_s^2 is signal variance.

Figure 14: The test data - a)the true image, b) the image degraded by matrix 5x5 and parameter σ=1, c) the image degraded by matrix 13x13 and parameter σ= 1.8

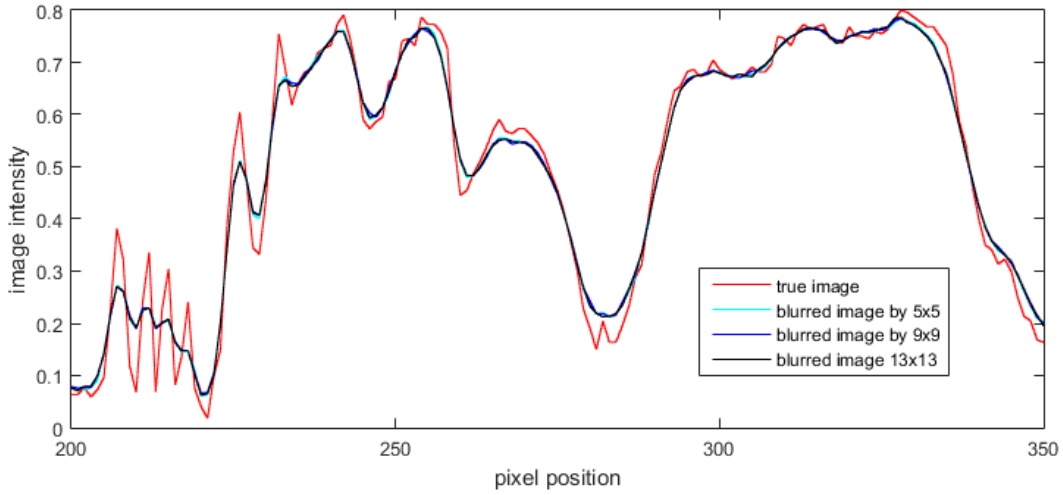

Figure 15: Comparison of the true test data image intensity and degraded data by the various matrix with parameter σ=1 sizes and noise

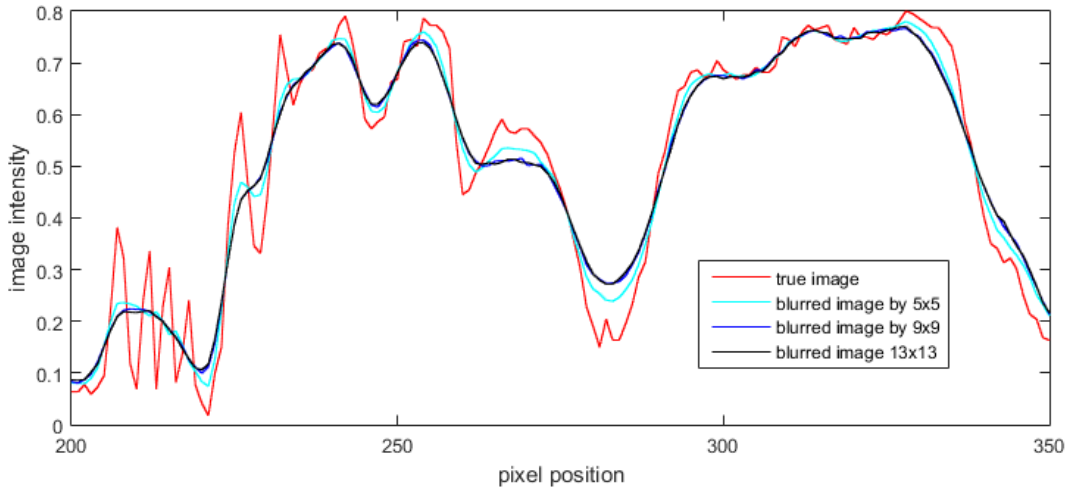

Figure 16: Comparison of the true test data image intensity and degraded data by the various matrix with parameter σ=1.8 sizes and noise

5.4 Built-in Matlab function (‘*deconvblind*’)

The proposed algorithm is compared with built-in Matlab function. This function reconstructs the true image using the maximum likelihood algorithm. Estimate of PSF and the true image is generated simultaneously, using an iterative process similar to the accelerated, damped Lucy-Richardson algorithm. The PSF restoration is strongly affected by initial guess PSF and less of the values its constraints. It is also strongly noise sensitive. That is why low noise level is used for the test data degradation [26].

5.5 Evaluation of results

Evaluation of image reconstruction efficiency is needed. There are two main approaches, the subjective and the objective. The subjective method is inconvenient, expensive and observer demanding. The objective method uses algorithms to evaluate restoration quality, which could be based on pixel difference measures (RMSE, SNR and PSNR), correlation measures, edge measures, sharpness measures, spectral distance measures or contrast measures.

5.5.1 Root mean square error

Root mean square error (RMSE) or mean square error (MSE) is a very common metric and is computed by averaging the squared difference between each pixel of the true image x and the reconstructed image y of size m x n. RMSE is used in most cases [14], [20], [25].

$$MSE = \frac{\sum_m \sum_n (y - x)^2}{m \cdot n} \tag{30}$$

$$RMSE = \sqrt{MSE} \tag{31}$$

5.5.2 Peak signal to noise ratio

Peak signal to noise ratio (PSNR) is another common metric, which is a variation of MSE and is computed as

$$PSNR = 20 \cdot \log_{10} \frac{max_x}{MSE}, \tag{32}$$

where max_x is maximum possible value in picture (equal 255 for 8-bit image). The value of PSNR is inversely proportional to image restoration quality [27].

SNR could also be computed from

$$SNR_{dB} = 10 \cdot \log_{10} \frac{\sigma^2_{signal}}{\sigma^2_{noise}}, \tag{33}$$

where the variance of signal and noise respectively is expressed by the σ^2.

5.5.3 Structural similarity index measure

Structural similarity index measure (SSIM) refers to difference and change in structural information between true and restored images. Luminance l, contrast c and structure s comparisons are computed separately.

$$l(x,y) = \frac{2\mu_x\mu_y + c_1}{\mu_x^2 + \mu_y^2 + c_1} \tag{34}$$

$$c(x,y) = \frac{2\sigma_x\sigma_y + c_2}{\sigma_x^2 + \sigma_y^2 + c_2} \tag{35}$$

$$s(x,y) = \frac{\sigma_{xy} + c_3}{\sigma_x\sigma_y + c_3} \tag{36}$$

$$SSIM(x,y) = [l(x,y)]^\alpha \cdot [c(x,y)]^\beta \cdot [s(x,y)]^\gamma \tag{37}$$

Where μ_x, σ_x^2 and $\sigma_x\sigma_y$ are average of image x, its variance and covariance of x and y. Constants c_1, c_2 and c_3 are determined in dependency on dynamic range of image and parameters α, β and γ determine influence of each component [28].

5.5.4 Image sharpness measure

The image sharpness measure allows the assessment of the image quality, without the reference image. That fact is very advantageous and necessary for assessment of the real data. The algorithm for this measurement has been proposed in [29]. The computation yield is to get the image quality measure FM, which expresses sharpness quality directly proportional.

$$T_M = |F| \tag{38}$$

T_M denotes the absolute value of Fourier transform of the assessed image and determine the $threshold = T_M/1000$. After computation of threshold it is necessary to define T_H as a number of pixels in F whose pixel value > $threshold$.

$$FM = \frac{T_H}{M \times N} \tag{39}$$

This assessing method is appropriate especially for blurred images and achieves better results than the best known image sharpness/blur measures [30] [31].

5.5.5 Contrast level measurement

Histogram Spread metric HS, proposed in [32], is used for contrast level measurement and could be also used as the evaluating criterion. This method is described by following equation and the quartiles are shown in Figure 17.

$$HS = \frac{Quartile\ distance\ of\ histogram}{Possible\ range\ of\ pixel\ values} = \frac{(3^{rd} quartile - 1^{st}\ quartile)\ of\ histogram}{(max - min) of\ the\ pixel\ value\ range} \quad (40)$$

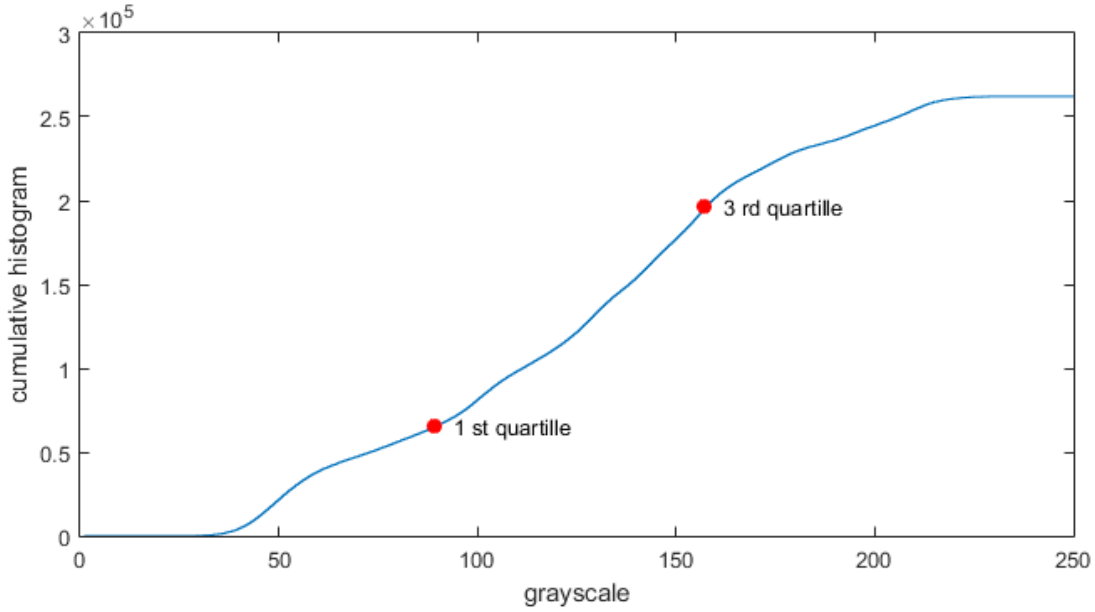

Figure 17: Cumulative histogram of the 'Lenna' image. Positions of the first and third quartile are marked.

5.6 Graphical user interface

The Graphical user interface in Matlab (GUI) is created for better algorithm access and settings. Figure 18 shows GUI window. In the left part of the window (Attachment A), it is possible to set up parameters of the chosen method and blur parameters. Blur parameters are defined by the kernel matrix size, sigma and additive noise is defined by SNR.

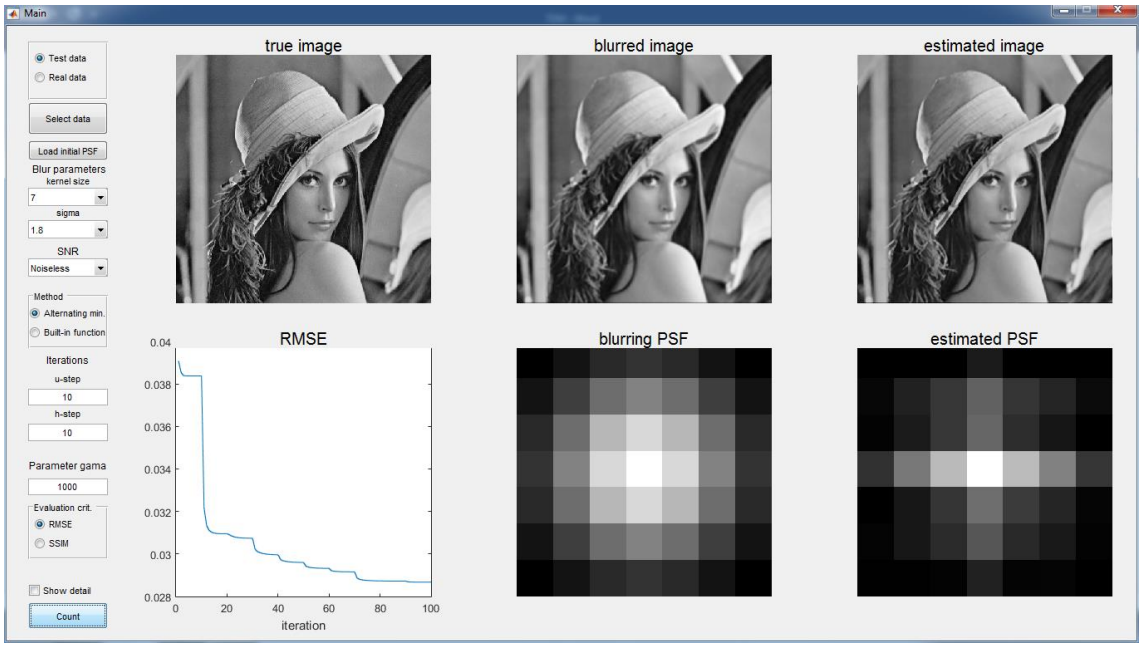

Figure 18: Graphical user interface

If the alternating minimization method is selected, it is displayed with a predefined number of *u*-steps and *h*-steps and the value of the parameter gamma, which can be modified. Furthermore, there is an option to choose the evaluating criterion. In the case that the test data is used, there are RMSE and SSIM criteria. Sharpness and contrast measurements are determined for the real data.

The first row of pictures shows the true data, the blurred data and the estimated data. In the second row is shown a graph of the evaluating criterion during iterations, the blurring PSF and the estimated PSF.

If the built-in Matlab function is selected, it is possible to set up ‘dampar’ and the number of iterations. The evaluating criterion during iterations is unfortunately unavailable.

The program also allows to show the detail of images, select your own test or real data and load initial PSF. In the case that PSF does not load, delta function is used for the alternating minimization algorithm and matrix of ones for built-in Matlab function.

6 Results

The proposed algorithm is tested on the test data and the real data according to the plan outlined in chapter 5.2.

First of all, it is necessary to set parameters γ and α. The parameters influence is tested and shown in the picture below. It is possible to see that with the low alpha and the high gamma parameter, the algorithm achieves the best level of RMSE. With respect to results shown in Figure 19 is parameter alpha set to $\alpha = 10^{-1}\gamma$, as is also proposed for SNR = 20 dB in Sroubek *et al.* [25]. However, our real data should not have such a low SNR, therefore the recommended setting of gamma is $\gamma = 1000$. In the graphical user interface is also possible to regulate the value of gamma parameter, which has to be non-zero.

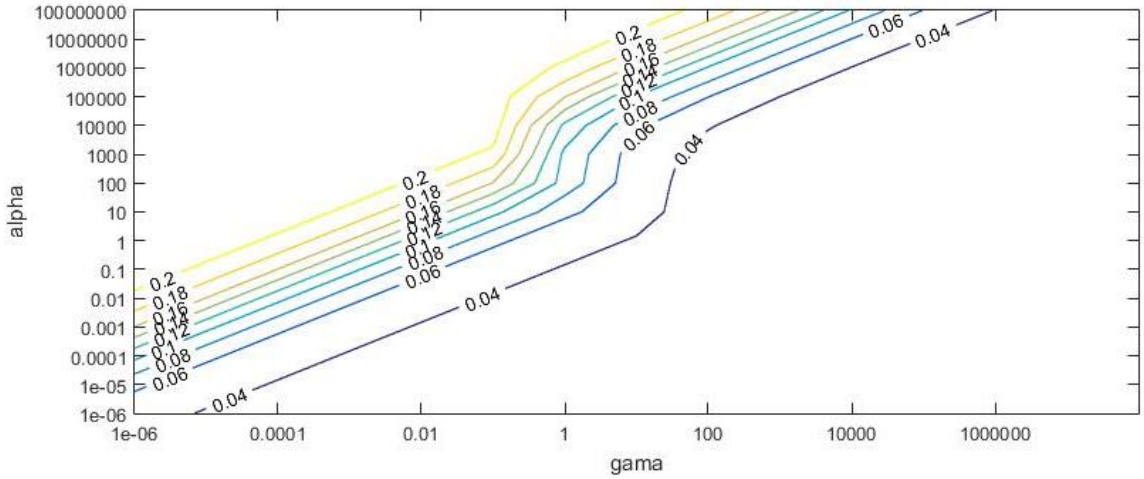

Figure 19: The lowest achieved RMSE with the appropriate set of parameters alpha and gamma

Delta function is used as the initial guess of PSF h_0, however, it is possible to load specific estimate.

The initial number of iterations of *u*-step is 10 and for the whole loop also 10. Thus the total number of iterations of *u*-step is 100.

6.1 Test data

The 'Lena' image, shown in the figure below, is used as the test data.

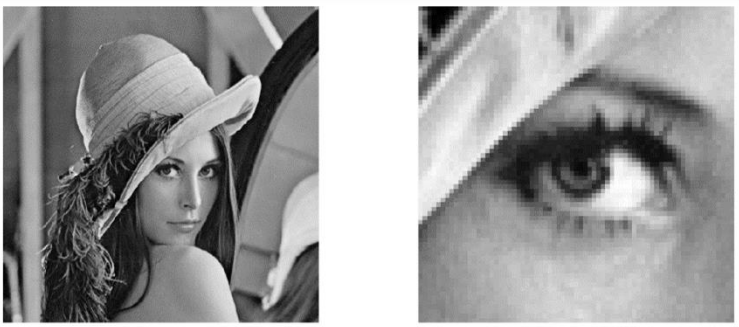

Figure 20: left - the original 'Lena' image, right - detail of the 'Lena' image

6.1.1 Noiseless case

The test data shown in Figure 21 in the first line are convolved with three different blurs (kernel size 5x5, 9x9 and 13x13 shown in the first line of Figure 22) with parameter $\sigma = 1.8$ and are noiseless. The alternating minimization algorithm results for 10 u-steps and 10 h-steps and parameter $\gamma = 1000$ are shown in the second line of Figure 21. The detail of the 'Lena' image is shown for better illustration of the results. The estimated PSFs are shown in Figure 22 in the second row. The difference is visible for example in distinguishable eyelashes, eye pupil or hat edge.

kernel size = 5	kernel size = 9	kernel size = 13
RMSE = 0.0263	RMSE = 0.0274	RMSE = 0.0322
SSIM = 0. 0.8434	SSIM = 0.8041	SSIM = 0.7986

Figure 21: Examples of the degraded test data by matrix 5x5, 9x9 and 13x13 in respective columns. The first row shows input degraded images and the second row shows the estimated images.

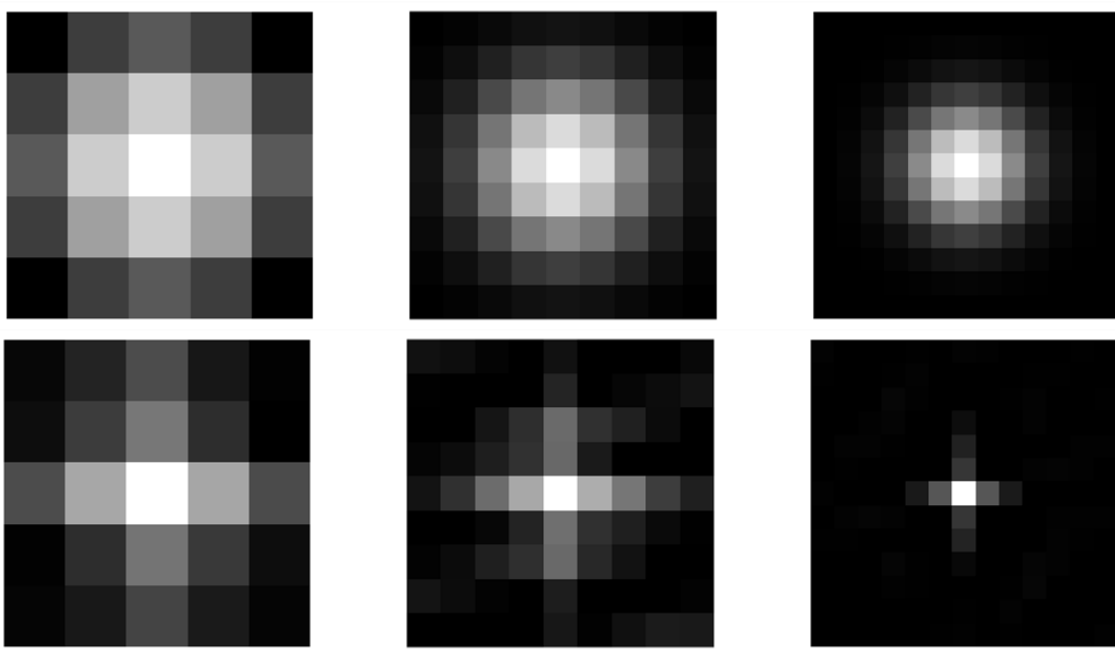

kernel size = 5 kernel size = 9 kernel size = 13

Figure 22: Examples of the blur matrix 5x5, 9x9 and 13x13 in respective columns. The first row shows used blurs and the second row shows the estimated ones

The image row detail is shown in Figure 23. Graphs in Figure 24 and Figure 25 show the dependency of RMSE and SSIM during 500 iterations (10 *u*-steps and 50 *h*-steps).

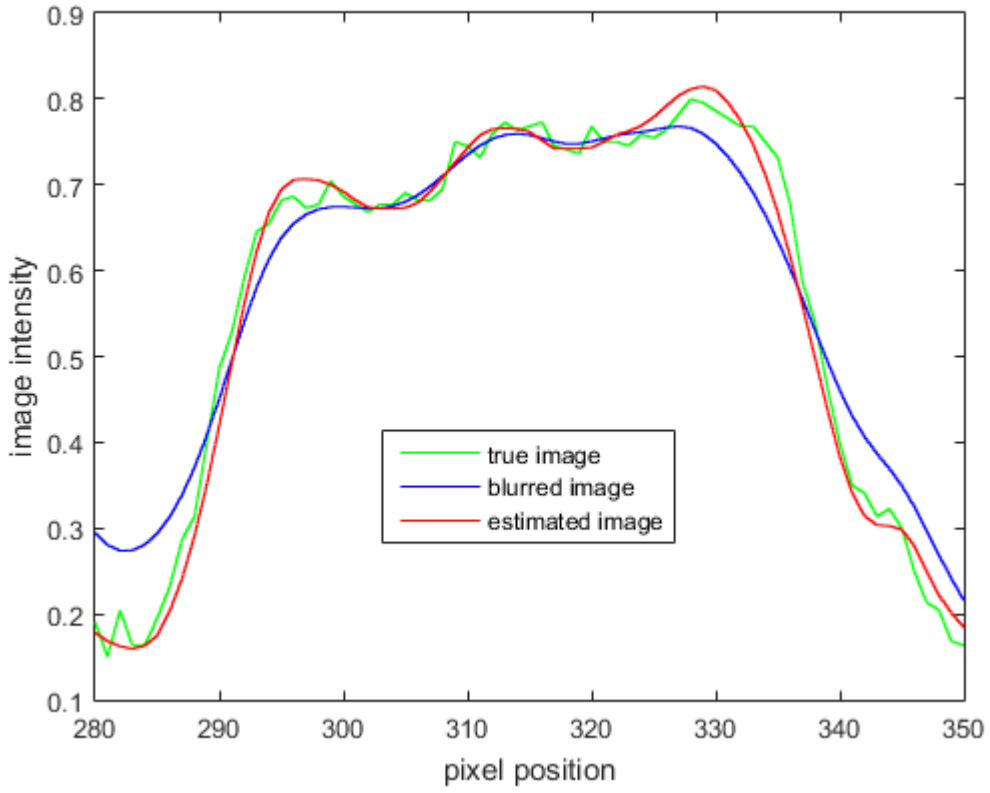

Figure 23: Estimated image amplitude compare to degraded (15 x 15 kernel size) and the true image

In Figure 23, it is visible that the estimated image intensity is much more similar to the true image than to the degraded image.

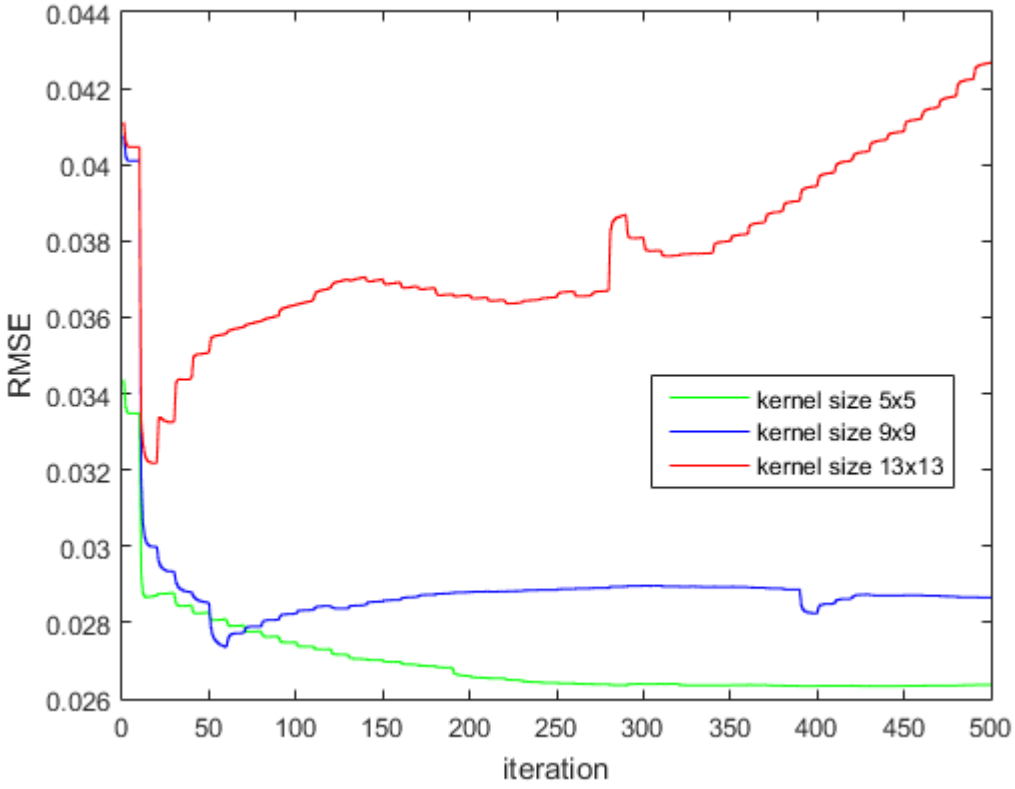

Figure 24: RMSE values for different kernel size during 500 iterations

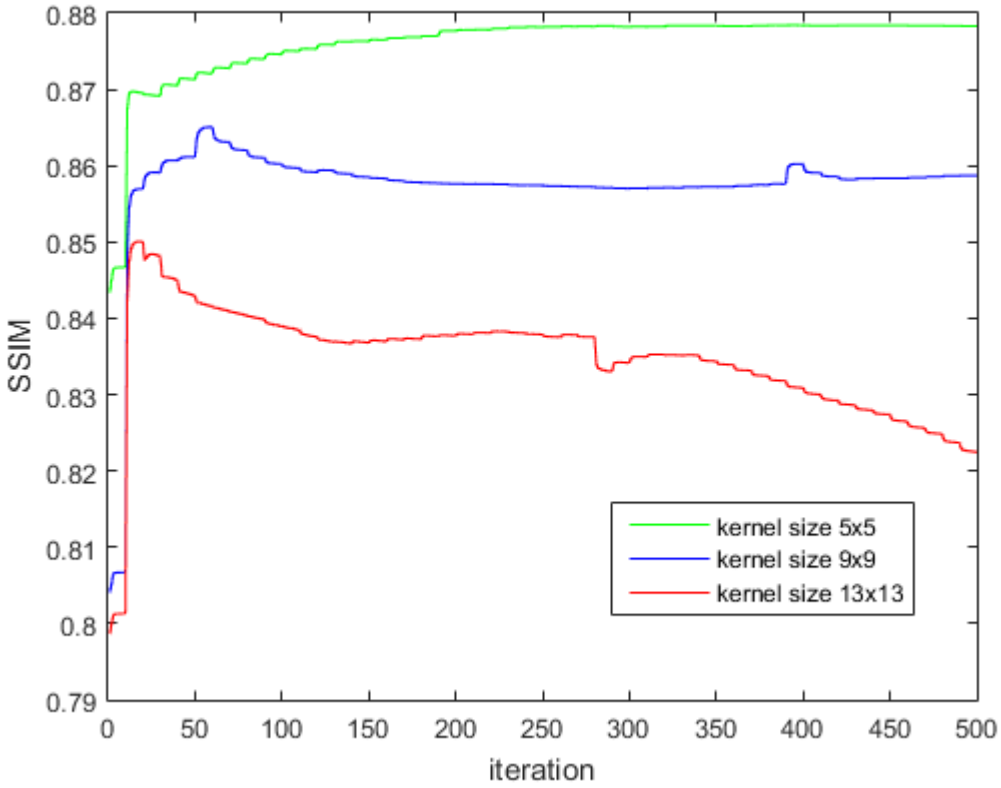

Figure 25: SSIM values for different kernel size during 500 iterations

In Figure 24 and Figure 25, it is possible to see, that the proposed method achieves better results with each iteration especially for smaller matrix sizes. For larger matrix sizes results degrade after some certain iterations.

6.1.2 Noisy case

The same process that is shown in the previous chapter is applied to the test data which are moreover degraded by the additive noise of SNR = 40 dB. Because the built-in Matlab function, which the algorithm will be compared, has high noise sensitivity, the lowest used SNR is 40 dB for better possibility of comparison (as was also proposed in [25]).

The first row of Figure 26 shows the degraded images by matrix sizes 5x5, 9x9 and 13x13 and in the second row the estimated images. Figure 27 shows the used PSFs and in the second row the estimated PSF. Parameter $\gamma = 1000$, 10 u-steps and 10 h-steps and delta function as the initial PSF guess is used to estimate the images.

kernel size = 5	kernel size = 9	kernel size = 13
RMSE = 0.0248	RMSE = 0.0272	RMSE =0.0326
SSIM = 0.8422	SSIM = 0.7954	SSIM = 0.3785

Figure 26: Examples of the degraded test data by matrix 5x5, 9x9 and 13x13 in respective columns. The first row shows the input degreaded images and the second row shows the estimated images.

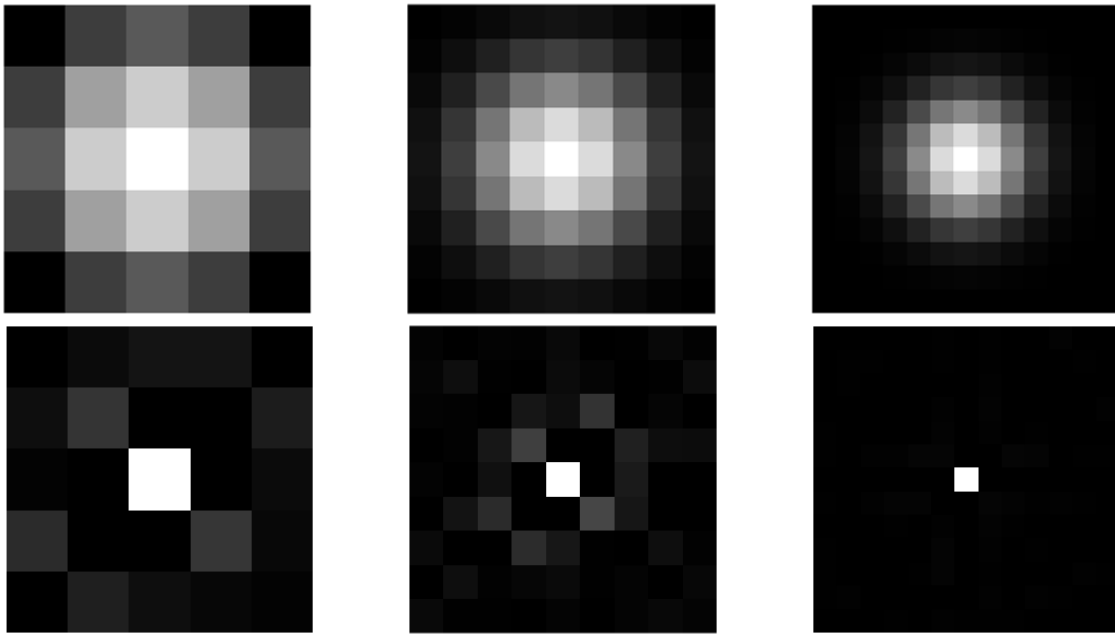

kernel size = 5	kernel size = 9	kernel size = 13

Figure 27: Examples of the blur matrix 5x5, 9x9 and 13x13 in respective columns. The first row shows used blurs and the second row shows the estimated ones

In Figure 27 it is possible to see, that estimated PSFs relatively differ from used PSF, although the image enhancement is apparent from Figure 28.

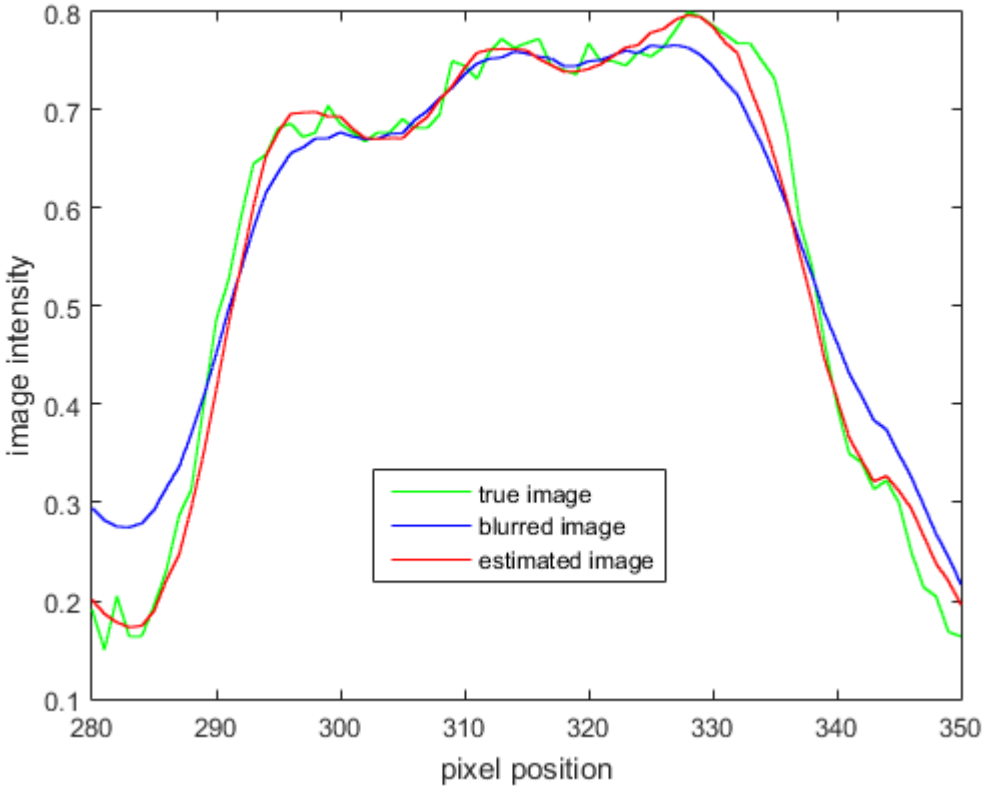

Figure 28: The estimated image amplitude compare to degraded (15 x 15 kernel size) and true image

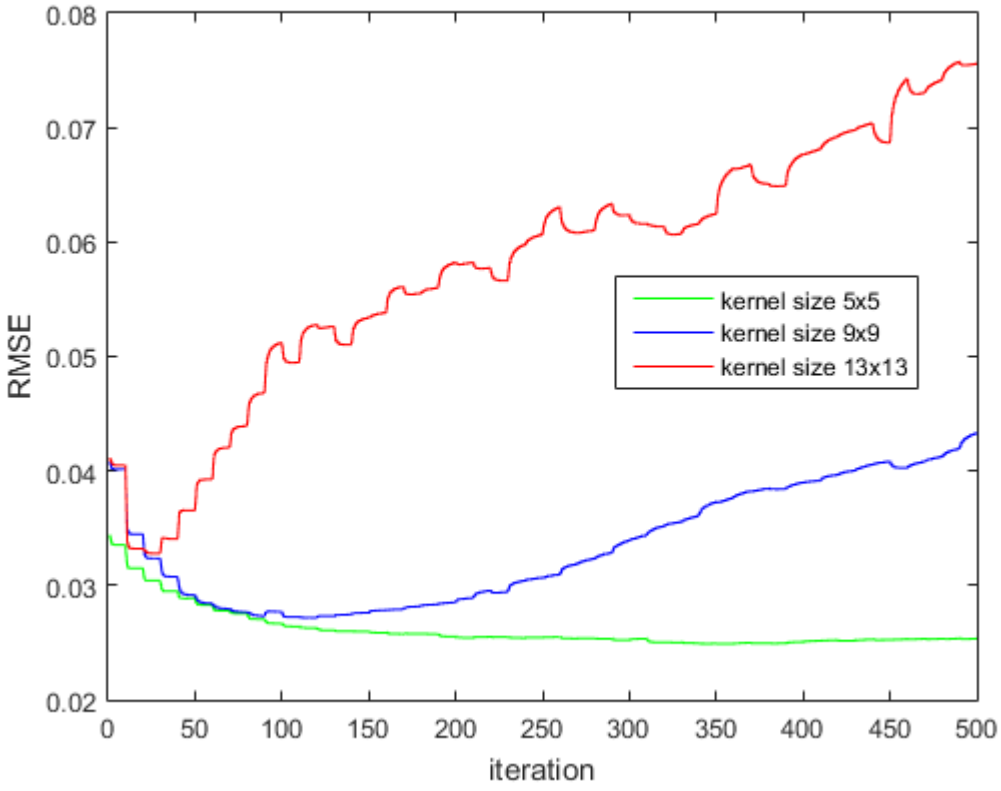

Figure 29: RMSE values for different kernel size during 500 iterations

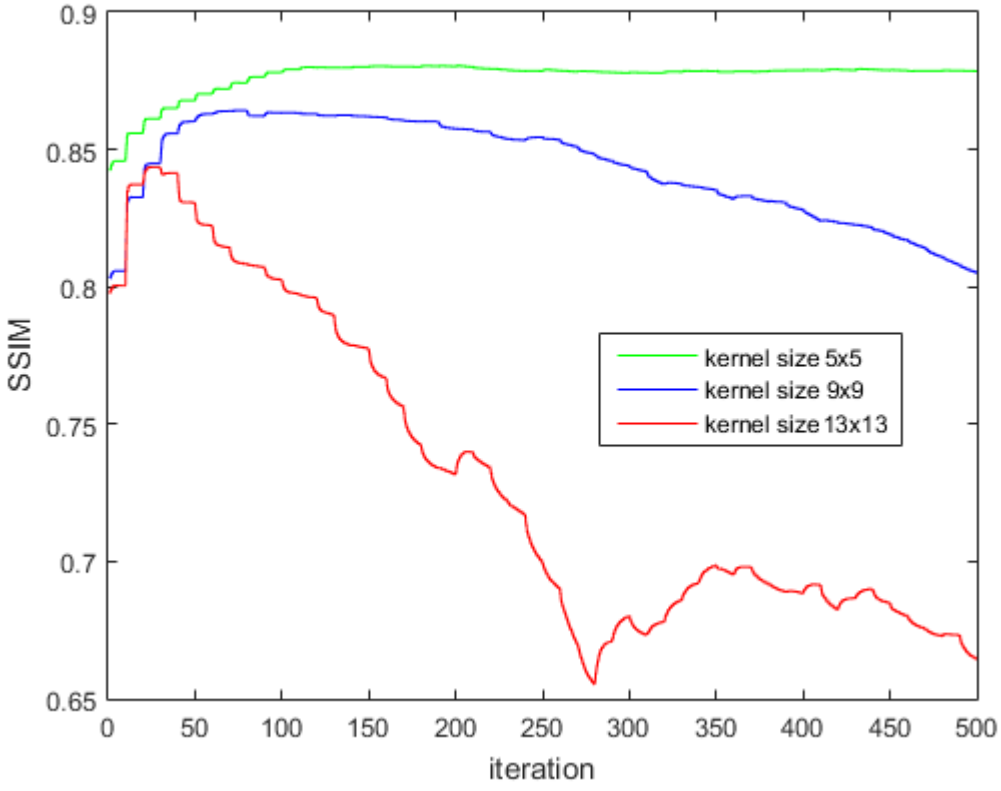

Figure 30: SSIM values for different kernel size during 500 iterations

Again it can be seen in Figure 29 and Figure 30, that the AM algorithm is not appropriate for the larger blurs and after several iterations, the estimate gets worse. It is possible to see that algorithm does not reach better results after 200 iterations.

6.1.3 Different data set

Another test data.is used for greater testing completeness. The test data is shown in Figure 31 and are convolved with three different blurs (kernel size 5x5, 9x9, and 13x13 and $\sigma = 1.8$) – the first row of Figure 32. The results of deblurring are in the second row of the same image. Parameter $\gamma = 1000$ and 10 u-steps and 10 h-steps are used. The 'cameraman' image is smaller (256 x 256 px) then the 'Lena' image (512 x 512 px) and has bigger amount of details.

Figure 31: The 'cameraman' image

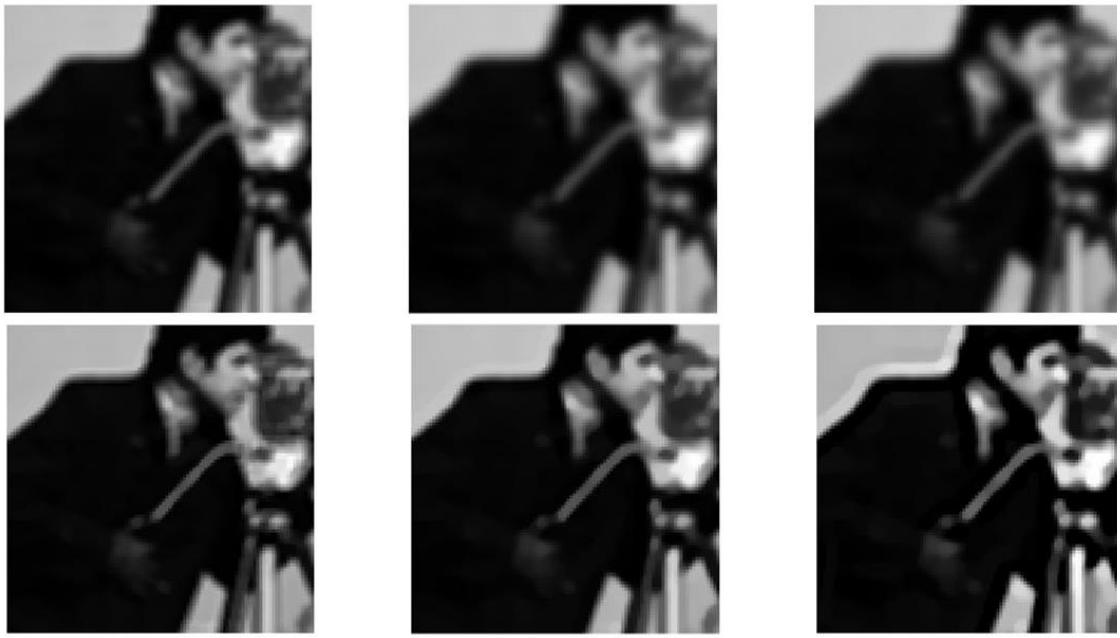

kernel size = 5
RMSE =0.0787
SSIM = 0.8108

kernel size = 9
RMSE = 0.0745
SSIM = 0.8022

kernel size = 13
RMSE = 0.0763
SSIM = 0.7858

Figure 32: Examples of the degraded test data by matrix 5x5, 9x9 and 13x13 in respective columns. The first row shows the input degraded images and the second row shows the estimated images.

Figure 32 shows obvious improvement of the image. The highest difference is visible on edges and in image details as is the cameraman's face or camera.

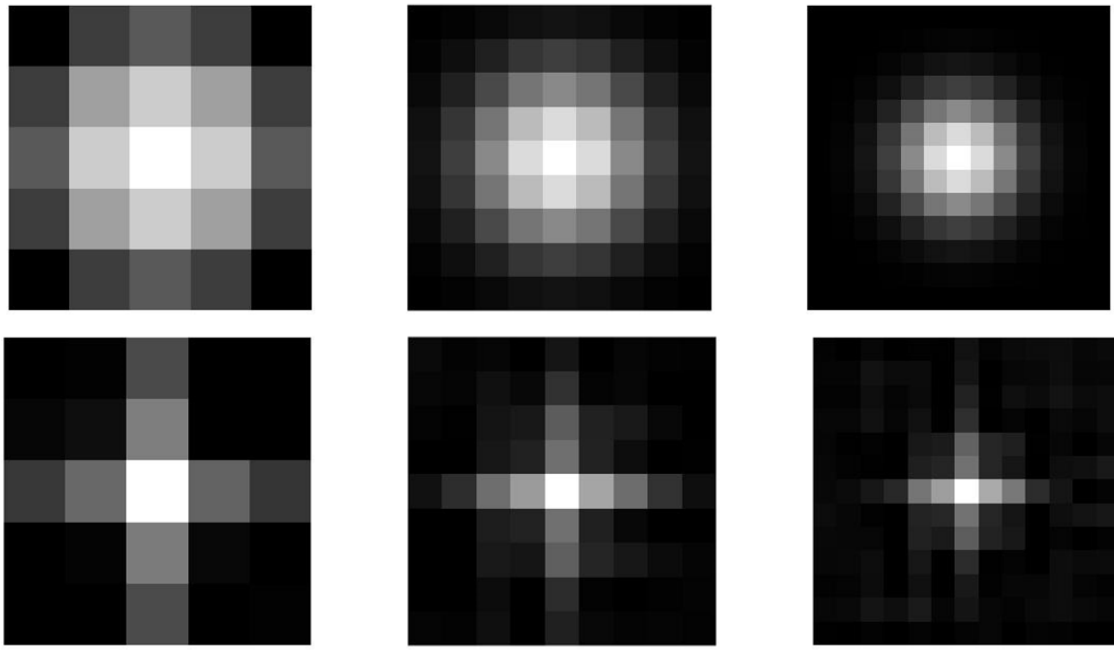

kernel size = 5 kernel size = 9 kernel size = 13

Figure 33: Examples of the blur matrix 5x5, 9x9 and 13x13 in respective columns. The first row shows used blurs and the second row shows the estimated ones

Although the estimated PSF, shown in Figure 33, is not exactly the same as is used for blurring, the image improvement is noticeably visible. That is proof of the algorithms functionality on different datasets.

6.1.4 Unsymmetrical PSF

For wider algorithm usage, it is necessary to know, if the algorithm is sensitive to unsymmetrical PSF. That aspect is tested in the following images. The test data is blurred by three different kernel sizes and unsymmetrical PSFs – the first row of Figure 34. The results of the algorithm are in the second row.

kernel size = 5	kernel size = 9	kernel size = 13
RMSE = 0.0289	RMSE = 0.0327	RMSE = 0.0334
SSIM = 0.8651	SSIM = 0.8351	SSIM = 0.8338

Figure 34: Degraded test data by matrix 5x5, 9x9 and 13x13 in respective columns. The first row shows input degraded images and the second row shows the estimated images

Figure 34 shows the visible difference between the degradeds mages and the estimated images. In Figure 35 is possible to see, that the AM algorithm can find even unsymmetrical PSF, unfortunately, the estimate is not very precise. Although the image has been improved.

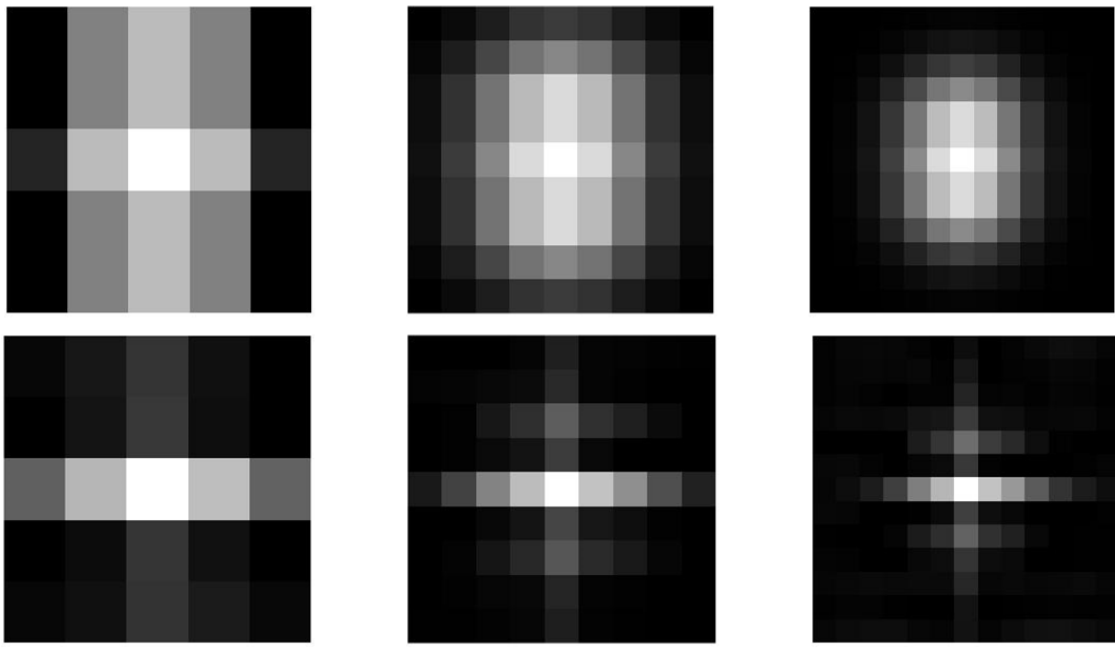

kernel size = 5	kernel size = 9	kernel size = 13

Figure 35: The unsymmetrical blur matrix 5x5, 9x9 and 13x13 in respective columns. The first row shows used blurs and the second row shows the estimated ones

6.1.5 Parameters testing

Figure 36 shows algorithm efficiency dependency on used blur. Efficiency is expressed by the lowest achieved RMSE during 100 iterations (the lowest values of RMSE corresponds to the best results). It is possible to see, that for lower values of the sigma parameter the algorithm succeeds better. The success of the algorithm relative to the

kernel size is dependent on the sigma parameter. Generally, it can be said that the method achieves the best results for a kernel size of around 10 pixels.

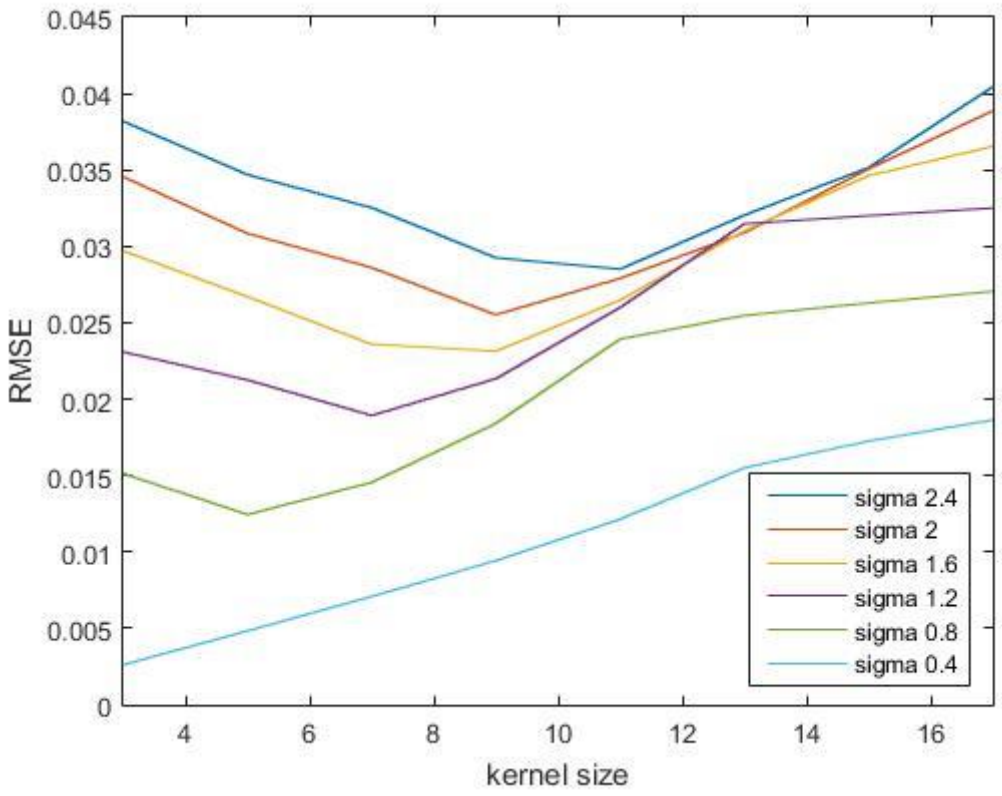

Figure 36: Algorithm efficiency for different blurs defined by kernel size and sigma

Furthermore, the method robustness is tested for overestimated and underestimated PSF. Figure 37 shows the dependency of the estimated image quality on estimated PSF size. It is observable, that in the case that sigma is low, the algorithm achieves better results when the kernel size is underestimated. Although for higher sigma parameter values, the algorithm reaches better results for overestimated PSFs. This dependency is not influenced by the size of blurring PSF.

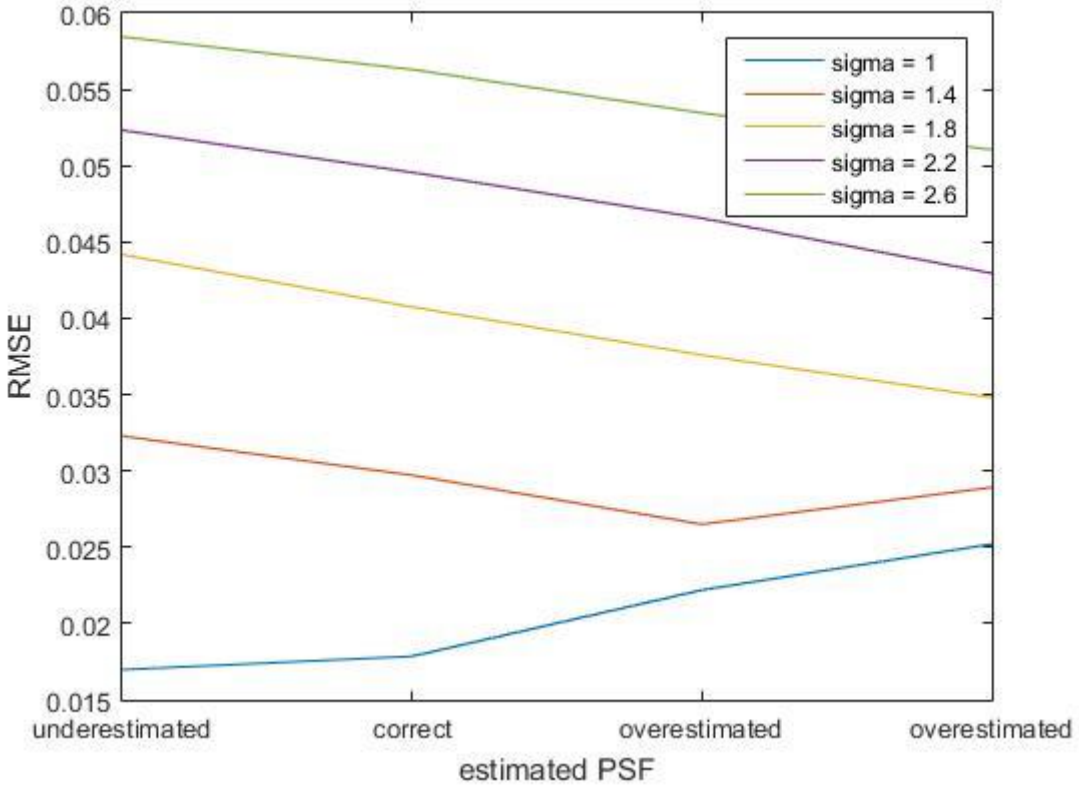

Figure 37: The image estimate quality dependency on estimated PSF size

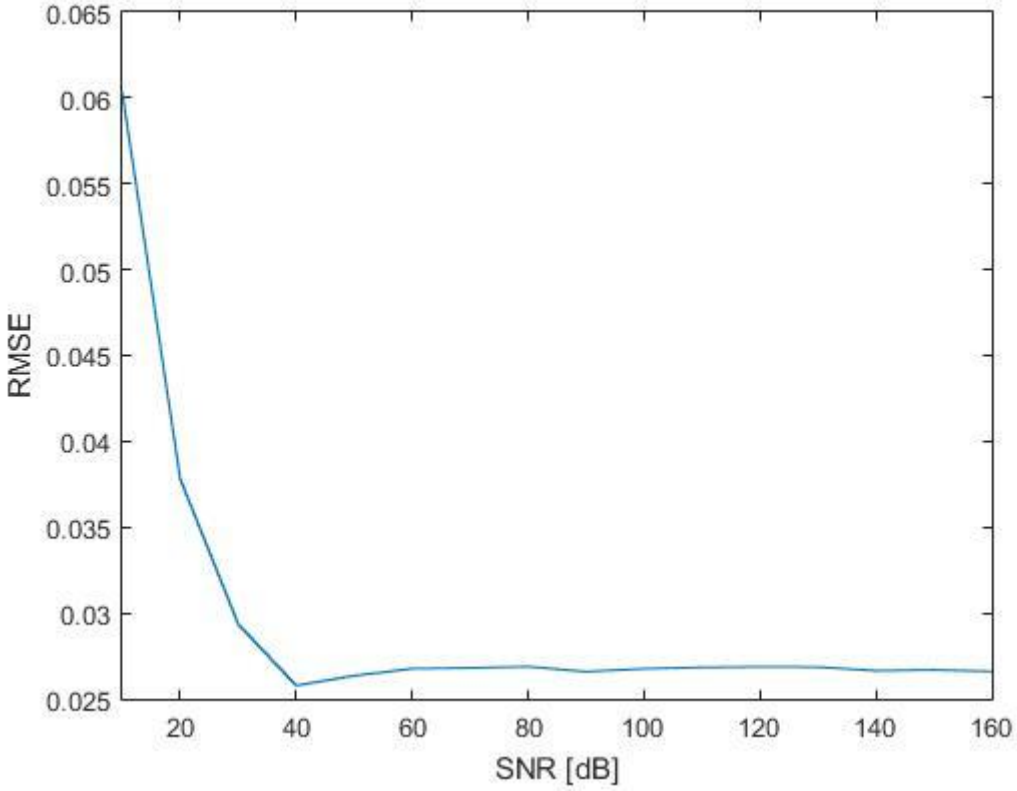

Figure 38: The image estimate quality dependency on SNR

In Figure 38 it is possible to see, that the AM algorithm is influenced by presences of noise. The SNR influence is tested with parameter $\gamma = 1000$ and 20 iterations of *h*-steps and 10 iterations of *u*-steps within one *h*-step. If the SNR is greater than 40 dB the method is capable of a relatively good estimate of the image and the PSF.

6.1.6 Built-in function

The same test data, as in the previous two chapters, is used for the built-in Matlab function testing. The blurred, noiseless test data are shown in the first row in Figure 39 and its corresponding estimates are shown in the second row. The estimate is generated after 10 iterations and the parameter 'dampar' is set to value 0.1.

The used PSFs (the first row) and the estimated PSFs (the second row) are shown in Figure 40.

kernel size = 5	kernel size = 9	kernel size = 13
RMSE = 0.1917	RMSE = 0.1905	RMSE = 0.1882
SSIM = 0.6436	SSIM = 0.6207	SSIM = 0.6170

Figure 39:Examples of the degraded test data by matrix 5x5, 9x9 and 13x13 in respective columns. The first row shows the input degraded images and the second row shows the estimated images.

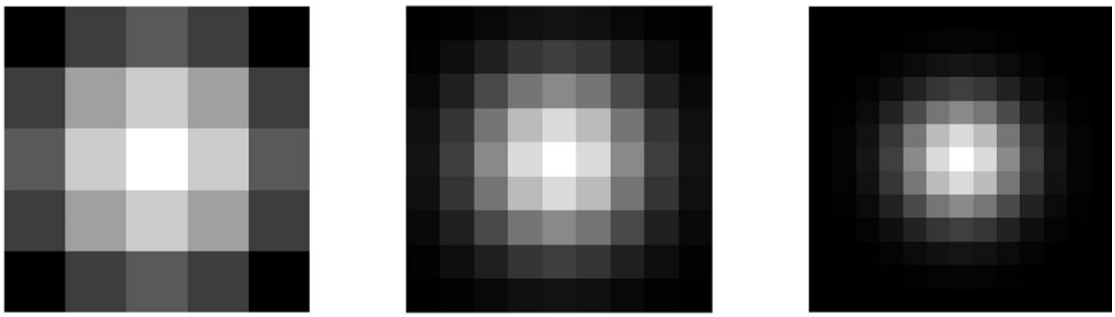

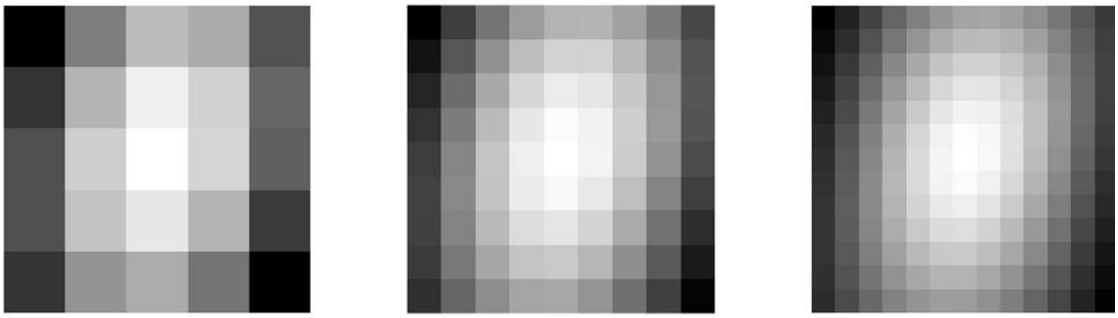

kernel size = 5 kernel size = 9 kernel size = 13

Figure 40: Examples of the blur matrix 5x5, 9x9 and 13x13 in respective columns. The first row shows used blurs and the second row shows the estimated ones

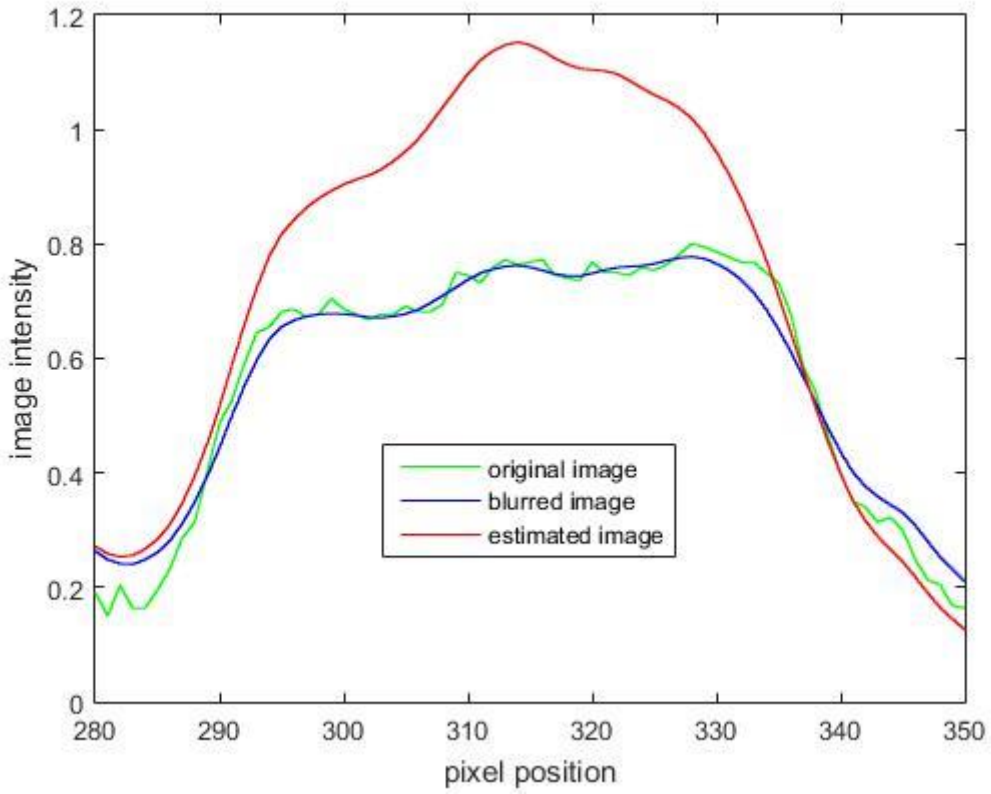

Figure 41: The estimated image amplitude compared to the degraded and the true image

Unfortunately, the results of the built-in feature are so bad that it was dropped from the next comparison. The inaccuracy of the estimate can be seen in Figure 41.

6.2 Real data

The real data were taken on a scanning transmission electron microscope with a LaB_6 gun filament from run at voltage of 120 kV. The chosen sample is a calibration standard for TEM – the gold polycrystalline on a carbon membrane.

The algorithm is tested for three different resolutions and two dwell times. The higher dwell time causes the lower noise. An appropriate resolution selection is very important.

From deconvolution theory, it is evident that the step of the electron probe should be smaller than the electron spot size. That the individual steps are overlapped and deconvolution is possible. It is realised from spot measurement, that spot size is approximately 2.4 nm. Therefore, magnification higher than 82 000 is sufficient. The used real data has magnification of 350 000x, 550 000x and 780 000x and is collected with the smallest possible spot size.

At first is necessary to define kernel size of the estimated PSF. The blur is unknown, hence an appropriate PSF is determined from image evaluation criteria. Figure 42 shows, that sharpness increases with increasing matrix size while the opposite is true for contrast, which decreases with a larger matrix size. Hence, a matrix of kernel size 5x5 is used for the following estimations.

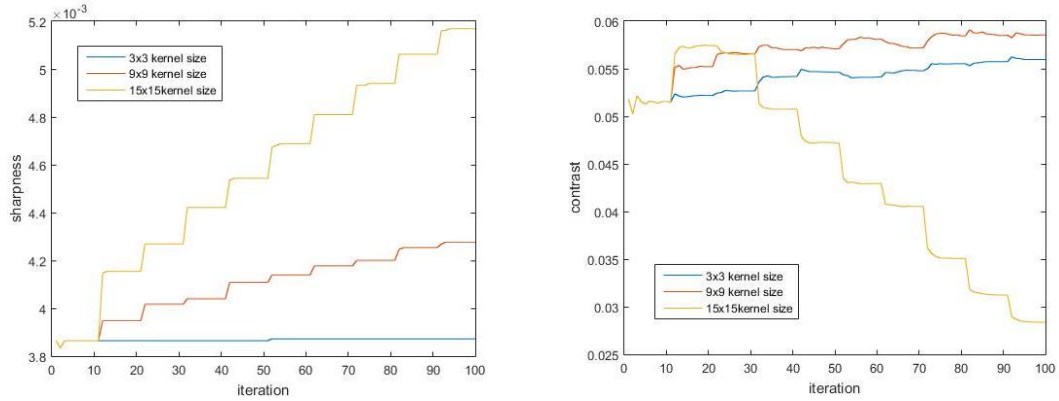

Figure 42: left- sharpness dependency on kernel size, right – contrast dependency on kernel size

Parameter γ is equal to 1000 and the total number of iterations is 200. The following groups of pictures demonstrate the algorithm results on the real data set. In each group, the input real data and the parameters are in the first column. In the second column is the sharpest version of the image estimate during the 200 iterations with the appropriate PSF estimate and in the third column is the highest contrast image estimate and the appropriate PSF. Delta function is subtracted from the PSF for better fluctuation visibility.

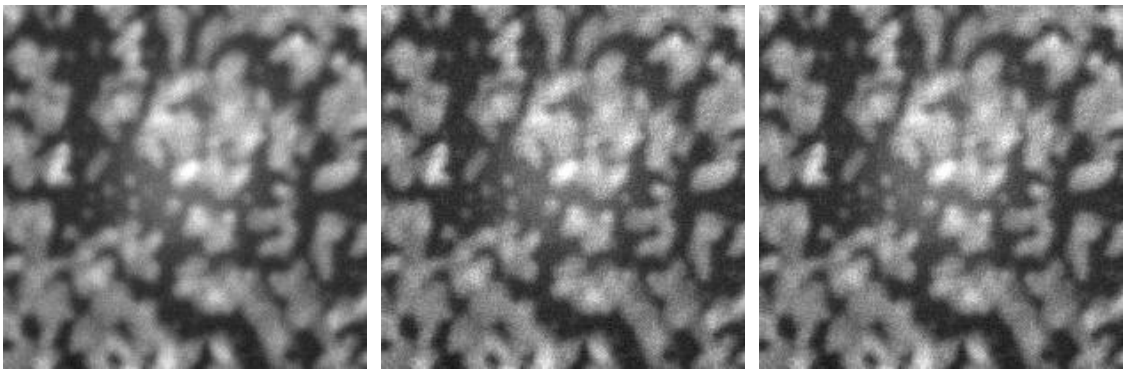

(a) (b) (c)

Magnification: 390 000x
Dwell time: 29 µs
Spot size: 11
Aperture: 50 µm

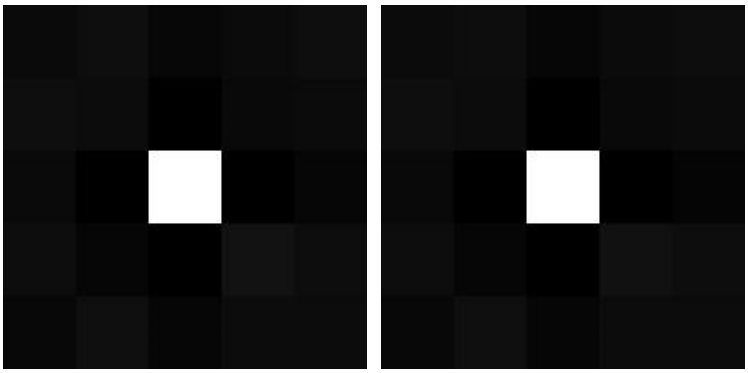

(e) (f)

Figure 43: (a) Real observed data. (b) The sharpest image estimate. (c) The most contrast image estimate. (e) Estimated PSF of the sharpest image estimate. (f) Estimated PSF of the most contrast image estimate.

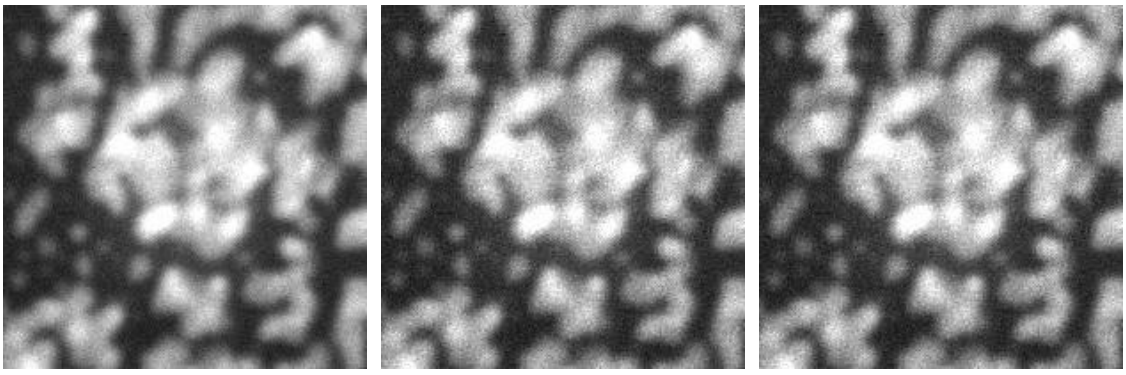

(a) (b) (c)

Magnification: 550 000x
Dwell time: 29 µs
Spot size: 11
Aperture: 50 µm

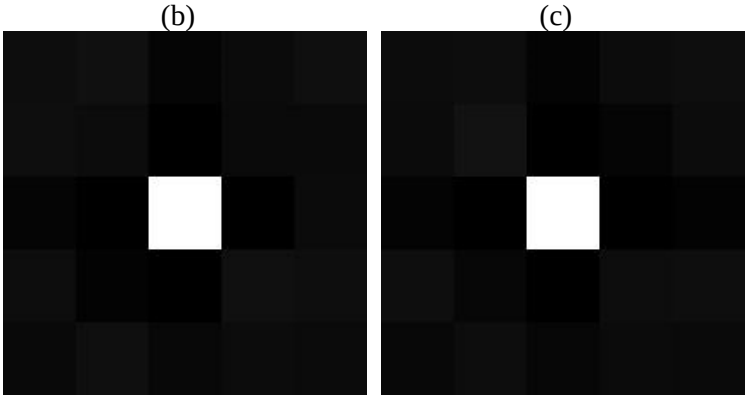

(e) (f)

Figure 44: (a) Real observed data. (b) The sharpest image estimate. (c) The most contrast image estimate. (e) Estimated PSF of the sharpest image estimate. (f) Estimated PSF of the most contrast image estimate.

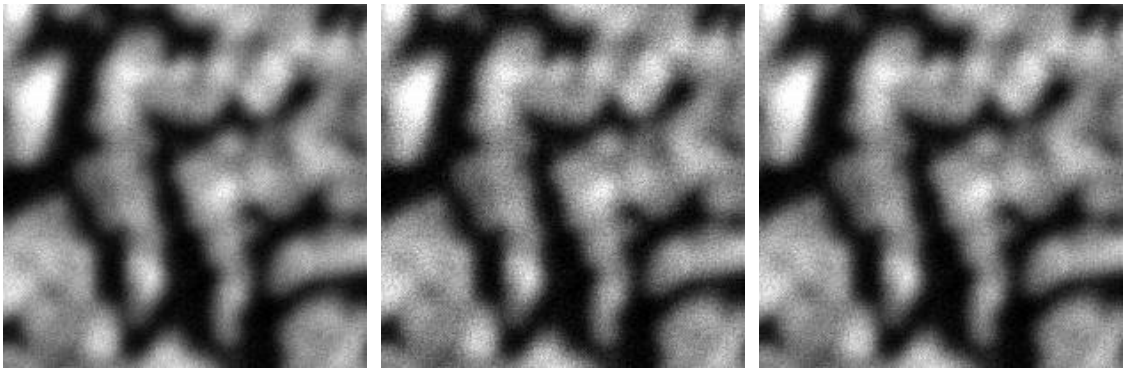

(a) (b) (c)

Magnification: 780 000x
Dwell time: 29 µs
Spot size: 11
Aperture: 50 µm

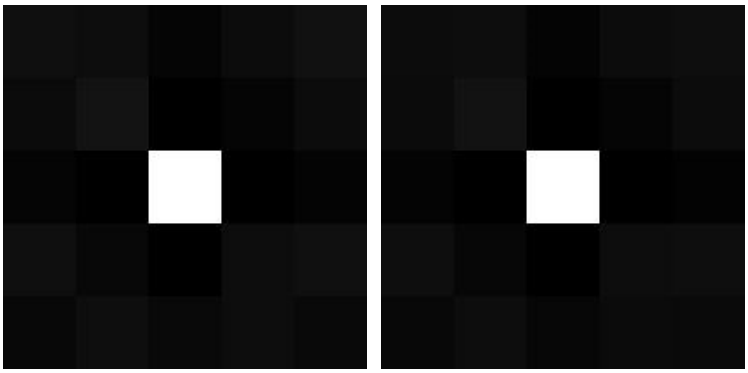

(e) (f)

Figure 45: (a) Real observed data. (b) The sharpest image estimate. (c) The most contrast image estimate. (e) Estimated PSF of the sharpest image estimate. (f) Estimated PSF of the most contrast image estimate.

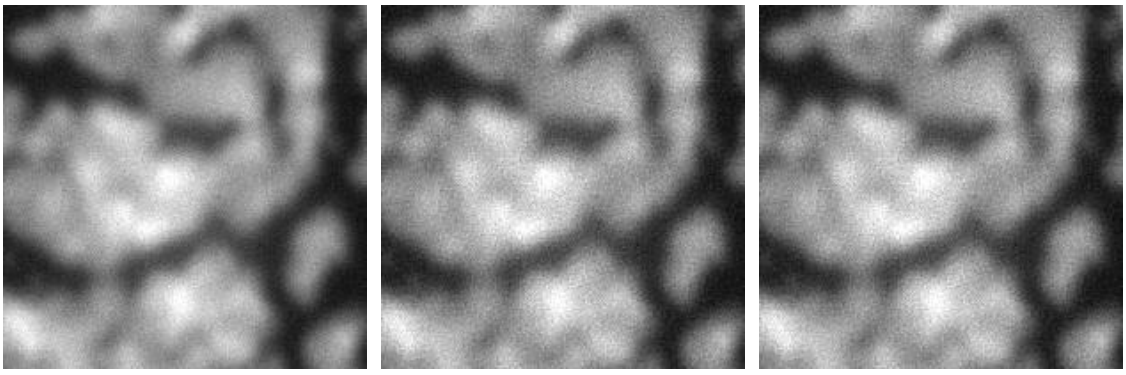

(a) (b) (c)

Magnification: 780 000x
Dwell time: 45 µs
Spot size: 11
Aperture: 50 µm

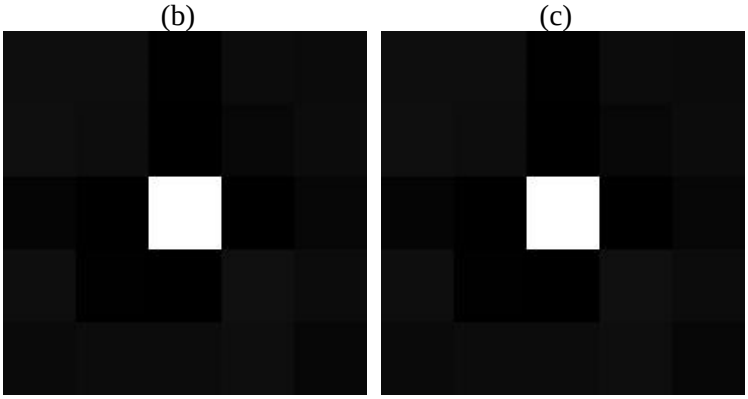

(e) (f)

Figure 46: (a) Real observed data. (b) The sharpest image estimate. (c) The most contrast image estimate. (e) Estimated PSF of the sharpest image estimate. (f) Estimated PSF of the most contrast image estimate.

From the previous pictures (Figure 43, Figure 44, Figure 45, and Figure 46) is possible to see that the proposed algorithm reaches a slight image improvement. Regrettably, the PSF estimate is extremely week.

Figure 47 shows the sharpness dependency on the magnification. The algorithm yields the better result with lower magnification. The contrast dependency on magnification is shown in Figure 48.

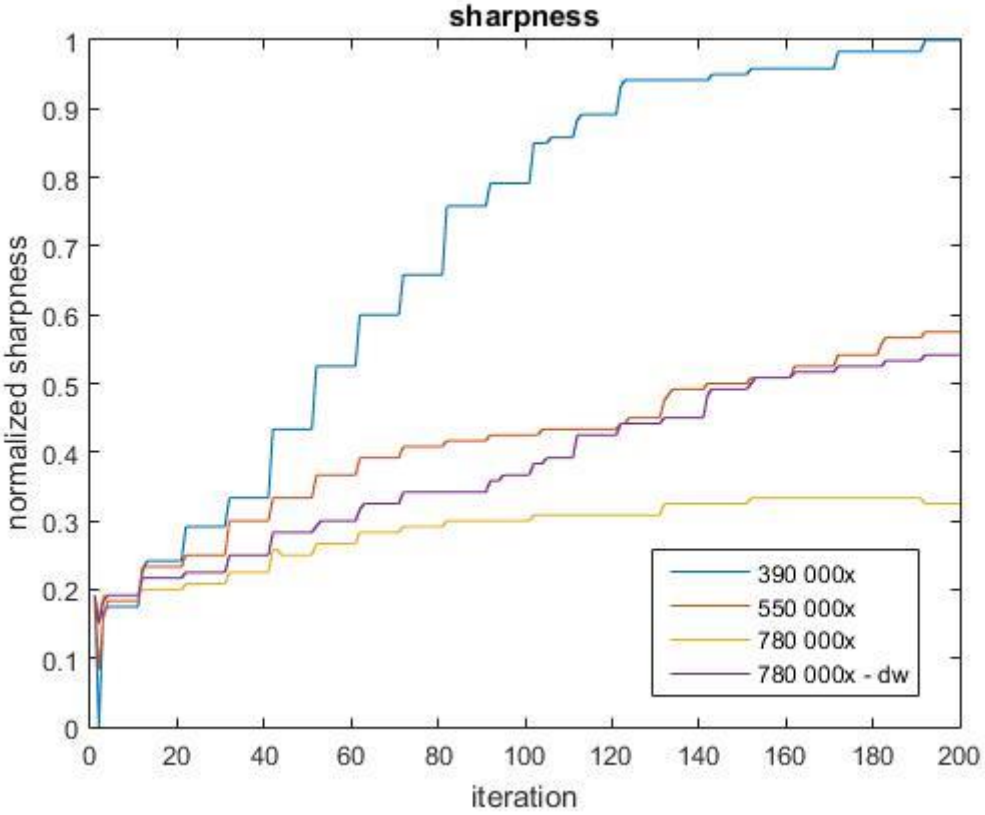

Figure 47: Sharpness dependency on magnification (780 000x - dw - denotes different dwell time)

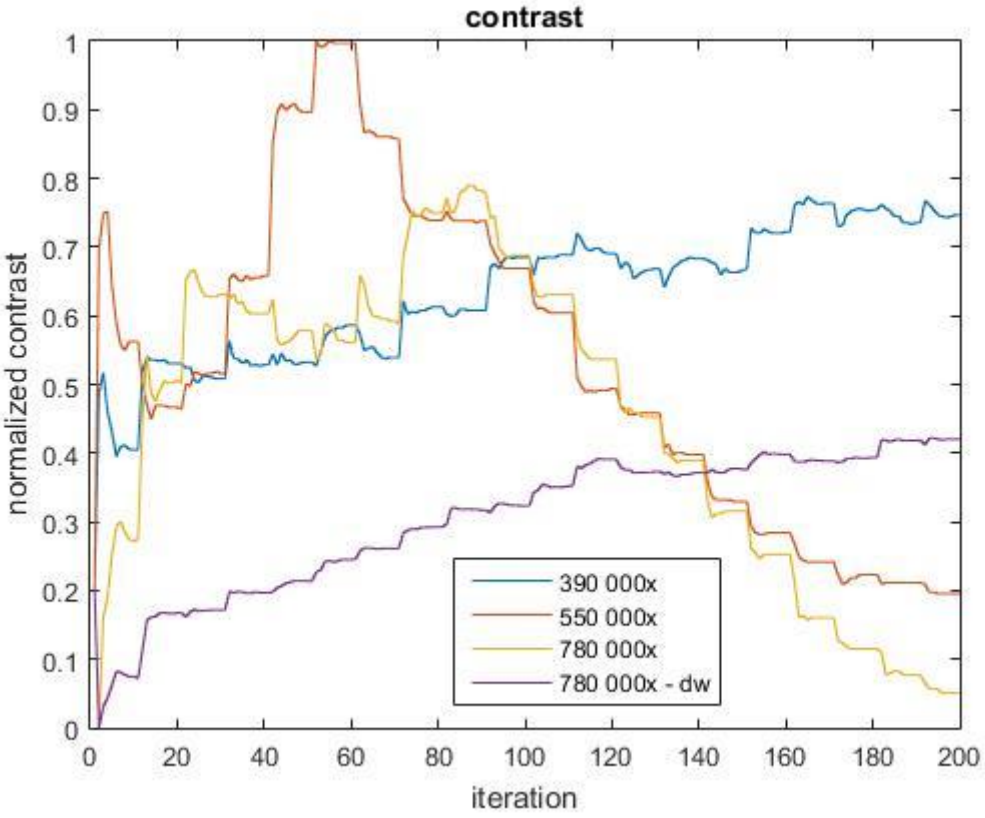

Figure 48: Contrast dependency on magnification (780 000x - dw - denotes different dwell time)

6.3 Discussion

Before the proposed algorithm application, it is necessary to set the parameters γ and α and estimate the kernel size of the blur. The different combinations of parameters γ and α are tested (see Figure 19) and based on this testing the alpha is set to a constant $\alpha = 10^{-1}\gamma$ and gamma is variable. For our data testing $\gamma = 1000$ is used.

The algorithm efficiency for different blurs is tested and it is obvious, that for larger blurs and larger sigma parameter the efficiency decreases. The same principle applies to SNR. From Figure 38 is evident, that the algorithm is inappropriate for SNRs lower than 40 dB. The algorithm is also not robust to overestimation or underestimation. The estimation dependency is shown in Figure 37. This is a considerable drawback in comparison with [25].

The image improvement is visible, although the algorithm is not capable to reconstruct the true data perfectly. The estimated PSF shape is similar, but not the same as the used blurs. The improvement is best seen visually and the RMSE and SSIM show convergence to optimum. The greatest difference between the degraded and the estimated image can be seen in image details and contrast edges.

Furthermore, it is observable that the algorithm does not achieve better results after 200 iterations. Moreover, the algorithm estimate for larger blurs degrades after numerous iterations.

The different dataset and different blurs shapes were is tried. Even in those cases, the image improvement is noticeable. Nevertheless, the difference between the true test data and the estimated image is in this case is quite high.

The algorithm inefficiency could be caused by inappropriate large blur. However, the ability to modify delta function to some blurs even far similar to the used blurs proves the algorithm functionality.

The built-in Matlab function does not reach any image improvement. The different setting of this function was tested, but none of the combination improves the image. The image degradation increases after each iteration, which was the reason why the built-in function is not even compared.

The algorithm functionality for the real data set is disputable. It is possible to see some difference between the input and output image, but the estimated PSF is almost equal to the delta function. Figure 49 shows the real data with marked line on the left side and the detail of the marked line on the right side. From this detail, it is possible to see, that the real data has the relatively high level of noise and are vastly blurred. As is tested before, this method is extremely noise sensitive. Hence, one of the reasons for the algorithm failure could be a high noise level in the input image. The next reason for inefficiency

could be the large blur of the observed image, that could cause irreversible information loss.

During the collection of the real data, an image degraded by condenser astigmatism was captured allowing the testing of the algorithm for unsymmetrical PSFs. This degradation should cause an unsymmetrical PSF. Unfortunately, on this data, even the approximate shape of the PSF has not been estimated.

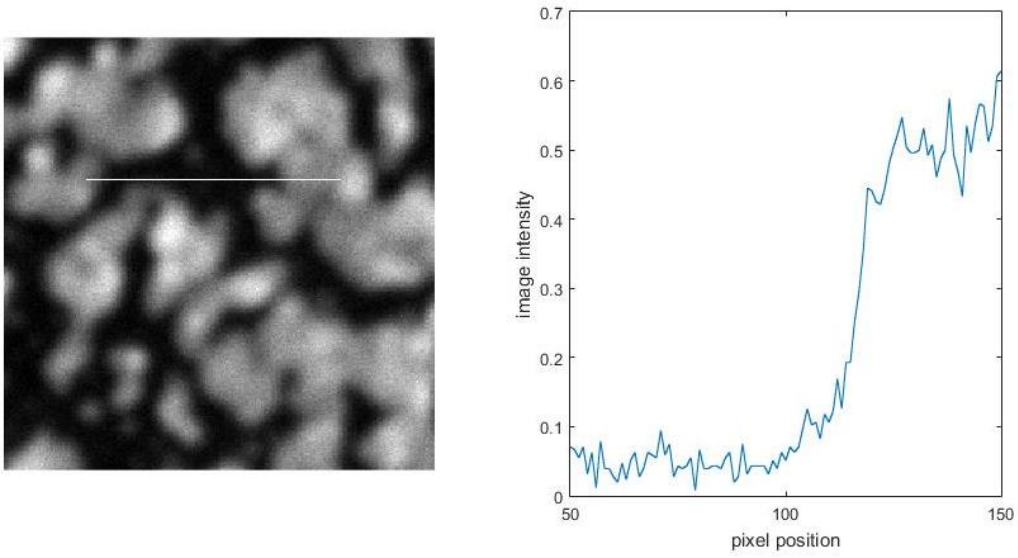

Figure 49: left - the real data, right - the marked line from the observed data image

For the next algorithm improvement can be used another or additional regularizators which are also suggested in [25]. *H*-step modification can be another alternation leading to improvement. One of the intended modification is to neglect the possible PSF unsymmetricity and in every *h*-step convolve the estimate with its rotation. Unfortunately, this modification would lead to information loss about the true shape of PSF (in case that the PSF is not symmetrical).

7 Conclusion

The blind deconvolution problem is an inverse and difficult problem to solve. One of the goal of this paper is to define distortion parameters, which is summarized in the first three chapters. There is also a description of TEM and STEM. Next chapter provides the overview of the most common blind deconvolution methods.

The next and main goal of this paper is to propose and apply blind image algorithm. The proposed method is described in the fifth chapter and the results are shown in the following chapter.

The proposed method is based on the alternating minimization for multichannel input as suggested in [25] and is modified to the singlechannel case.

From testing results, it is obvious that the proposed algorithm is functionable. Nevertheless, has numerous limitations. It's efficiency significantly decrease with large blurs, low SNR, inappropriate set up of parameters gamma or incorrect PSF size estimates. This is a significant drawback in comparison with the suggested method in [25]. The algorithm functionality is clearly visible on the test data results and from the RMSE and SSIM values.

Due to inadequate results from built-in Matlab function, the planned comparison was dropped out.

Unfortunately, the improvement is minimal for the real data. That can be caused by low SNR or large blur, causing image information loss. The proposed algorithm improvements are suggested in section discussion.

The algorithm is applicable for images with small blurs (small kernel size and low sigma) and high SNR. Its advantage is also low computing time and capability of large image processing, thus implementation in the frequency domain.

Bibliography

1. Erni R. *Aberration-corrected imaging in transmission electron microscopy: an introduction.* Hackensack, NJ : Distributed by World Scientific Pub. Co., 2010. ISBN 978-1-84816-536-6.

2. Kubínek R., Šafářová K., Vůjtek M. *Elektronová mikroskopie.* Olomouc : Univerzita Palackého v Olomouci, 2011. ISBN 978-80-244-2739-3.

3. Goodhew P. J., Humphreys F. J., Beanland R. *Electron microscopy and analysis. 3rd ed.* New York : Taylor & Francis, 2001. ISBN 0-7484-0968-8.

4. Microscopic techniques. *NPTEL.* [Online] 5/ 16, 2018. http://nptel.ac.in/courses/102103044/module3/lec17/3.html.

5. Karlík M. *Úvod do transmisní elektronové mikroskopie.* Praha : České vysoké učení technické v Praze, 2011. ISBN 978-80-01-04729-3.

6. Zuo J. M., Spence J. C. H. *Advanced transmission electron microscopy.* New York : Springer New York, 2017. DOI: 10.1007/978-1-4939-6607-3 ISBN: 9781493966059.

7. Yasuda K., Shigekazu U., Hideho G. Properties of a YAP powder scintillator as alpha-ray. *Applied Radiation and Isotopes.* 2000, Vol. no. 3, 52. p 365-368, ISSN: 0969-8043 ; DOI: 10.1016/S0969-8043(99)00179-7 .

8. Equeenuddin S. M., Pattnaik B. K. Assessment of heavy metal contamination in sediment at Sukinda ultramafic complex using HAADF-STEM analysis . *Chemosphere.* 2017, 185. pp. 309-320, ISSN: 0045-6535 ; DOI: 10.1016/j.chemosphere.2017.06.131 .

9. Vyšín I., Říha J. *Paprsková a vlnová optika.* Olomouc : Univerzita Palackého v Olomouci, 2012. ISBN 978-80-244-3334-9 .

10. Pennycook S. J., Lupini A. R., Varela M., et al. Scanning transmission electron microscopy for nanostructure characterization. *Scanning microscopy for nanotechnology: techniques and applications.* New York : Springer, 2007. ISBN 0-8493-7367-0.

11. Campisi P., Egiazarian K. *Blind image deconvolution: theory and applications.* Boca Raton : CRC Press, 2007. ISBN 0-8493-7367-0.

12. Joshi N., Szeliski R., Kriegman D. J. PSF estiamtion using sharp edge predicion. *IEEE Conference on Computer Vision and Pattern Recognition.* 2008, pp. 1-8.

13. Ghiglia D. C., Romero L. A., and Mastin G. A. Systematic approach to two-dimensional blind deconvolution by zero-sheet separation. *Journal of the Optical Society of America A.* 1992, Vol. 10, pp. 1024-1036.

14. Kundur D., Hatzinakos D. Blind image deconvolution. *IEEE Signal procesing magazine.* 1996. p. 43 - 64, ISSN: 1053-5888 ; DOI: 10.1109/79.489268 .

15. Premaratne P., Ko C. C. Zero sheet separation of blurred images with symmetrical point spread functions. *Conference Record of the Thirty-Third Asilomar Conference on Signals, Systems, and Computers.* 1999, 2. p. 1297 - 1299, ISSN: 1058-6393 ; ISBN: 0-7803-5700-0 ; DOI: 10.1109/ACSSC.1999.831916.

16. Chen F., Ding F., Sheng J. Maximum likelihood based recursive parameter estimation for controlled autoregressive ARMA systems using the data filtering technique. *Journal of the Franklin institute.* 2015, 352. p. 5882 - 5896, ISSN 0016-0032.

17. Zhipo D., Youshen X. A neural network algorithm for fast blind image restoration using 2D-ARMA paramter estimation. *2010 International Conference on Audio, Language and Image Processing.* Fuzhou, China : Fuhou University, 2010. ISBN: 978-1-4244-5856-1 ; E-ISBN: 978-1-4244-5857-8 ; E-ISBN: 978-1-4244-5858-5 ; DOI: 10.1109/ICALIP.2010.5685204 .

18. Geman D., Reynolds G. Constrained Restoration and the Recovery of Discontinuities. *IEEE Transactions on Pattern Analysis and Machine Intelligence.* 1992, Vol. 14, no. 3. , p. 367 - 383, ISSN: 0162-8828 ; DOI: 10.1109/34.120331 .

19. Bouhamidi A., Jbilou K. Sylvester Tikhonov-regularization methods in image restoration. *Journal of Computational and Applied Mathematics.* 2007, 206. pg. 86-98, ISSN: 0377-0427 ; DOI: 10.1016/j.cam.2006.05.028 .

20. Gholami A., Hosseini S. M. A balanced combination of Tikhonov and total variation regularizations for reconstruction of piecewise-smooth signals. *Signal processing.* 2013. ISSN: 0165-1684 ; DOI: 10.1016/j.sigpro.2012.12.008.

21. Wong C., Chan T. Total variation blind deconvolution. *IEEE Transactions on Image Processing.* 1998, Vol. 7, 3, pp. 370 - 375.

22. Liu A. Blind image deconvolution. [Online] 2014. [Cited: 12/ 17, 2017.] http://www.dartmouth.edu/~aron/Image%20Deconvolution%20-%20Aron%20Liu.pdf.

23. Ayers G. R., Dainty J. C. Iterative blind deconvolution method and its applications. *Optics Letters.* 1988, Vol. 13, 7.

24. Chen Y., Enokura T., Nakao Z. A fast image restoration algorithm base on simulated annealing. *Third International Conference on Knowledge-Based Intelligent Information Engineering Systems.* 1999. p. 341- 344, ISBN: 0-7803-5578-4 ; DOI: 10.1109/KES.1999.820193.

25. Šroubek F., Milanfar P. Robust multichannel blind deconvolution via fast alternating minimization. *IEEE Transactions on image processing.* 2012, Vol. 21, no. 4. p. 1687-1700, DOI:10.1109/TIP.2011.2175740.

26. MathWorks®. *Documentation R2017b.* [Online] [Cited: 2/ 1, 2018.] https://www.mathworks.com/help/images/ref/deconvblind.html.

27. Al-Najjar Y. A. Y., Soong D. C. Comparison of image quality assessment: PSNR, HVS, SSIM, UIQI. *International journal of scientific & engineering research.* 2012, 3. ISSN: 2229-5518.

28. Wang Z. Image qualit assessment: From error visibility to structural similarity. *IEEE Transactions on image procesing.* 2004, Vol. no. 4, 13. p. 600 - 612, ISSN: 1057-7149 ; E-ISSN: 1941-0042 ; DOI: 10.1109/TIP.2003.819861 .

29. De K., Masilamani V. Image sharpness measure for blurred images in frequency domain. *Procedia Engineering 64.* 2013, pp. 149-158.

30. Narvekar N., Karam L. J. An improved no-reference sharpness metric based on the probability of blur detection. *Workshop on Video Proc. And Quality Metrics.* 2010.

31. Ferzli R., Karam L. J. A No-reference Objective Image Sharpness Metric based on the notion of Just Noticable Blur (JNB). *IEEE Transactions on Imae Processing.* Vol. 18, 4, pp. 717-728.

32. Tripathi A. K., Mukhopadhyay S., Dhara A. K. Performance Metrics for Image Contrast. *International Conference on Image Information Processing.* 2011.

33. MathWorks®. *Deblur with the blind deconvolution algorithm - Documentary R2017b.* [Online] 1/ 4, 2018. https://www.mathworks.com/help/images/deblur-with-the-blind-deconvolution-algorithm.html.

Abbreviations

ADF	Annular dark-field
AM	Alternating minimization
AR	Autoregressive
ARMA	Autoregressive moving average
BD	Blind deconvolution
BF	Bright-field
CCD	Charged couple device
GUI	Graphical user interface (in Matlab)
HAADF	High-angle annular dark-field
LDS	Linear degradation system
MA	Moving average
ML	Maximum-likelihood
MSE	Mean square error
PSF	Point spread function
PSNR	Peak signal to noise ratio
RMSE	Root mean square error
SEM	Scanning electron microscope
SSIM	Structural similarity index measure
STEM	Scanning transmission electron microscope
TEM	Transmission electron microscope
TV	Total variation

Attachment

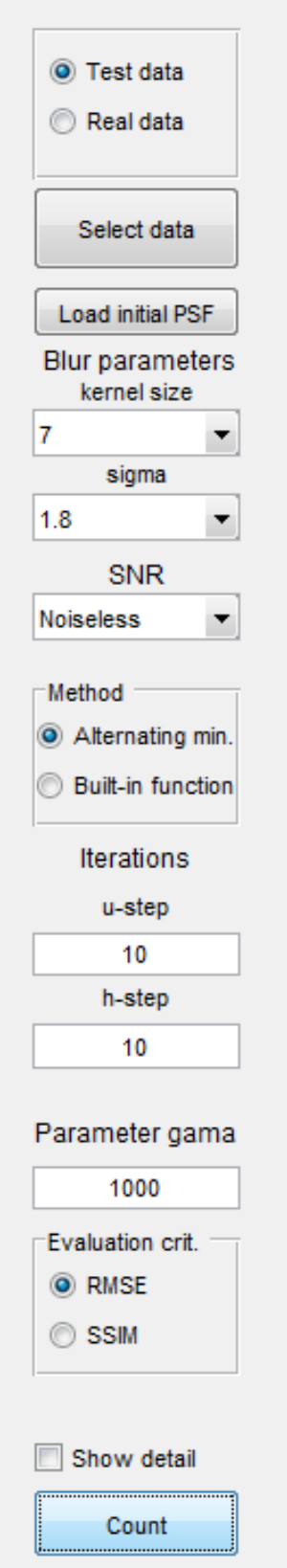

Attachment A: GUI detail